LOCAL REARRANGEMENT AND MICROMECHANICAL COMPARISONS BETWEEN SHEAR BANDS AND SIMPLE SHEAR IN GRANULAR MATERIALS

by
Surya Sidhartha Kolluri

A thesis submitted to the Johns Hopkins University in conformity
with the requirements for the degree of Master of Science in Engineering

Baltimore, Maryland
May 2022

Abstract

We see granular materials all around us in nature and industry in landslides, sand, avalanches and in medical pills and food processing industries. Given their ubiquity, their inelastic and critical state behaviour is of great interest. We compare an experimentally generated shear band in a granular material (Ottawa sand) and a discrete element simulation of a granular material under simple shear from the lens of local rearrangements. Experiments utilizing sophisticated imaging capabilities in geomechanics have enabled direct observation of strain localization mechanisms that lead to the formation of shear bands during the deviatoric loading of granular materials. These experiments involve combining mechanical testing with modern X-ray computed micro-tomography imaging and using robust DIC algorithms [1, 2]. These grain scale experiments have helped directly observe and capture the mechanics of the shear band from its inception until it is fully formed [3, 4]. However, local rearrangements within shear bands have not been quantified and extensively studied. There have also been micromechanical studies of simple shear flow in granular materials to understand microscopic plastic deformations [5, 6, 7]. However, a direct micromechanical and local rearrangement comparison of these two similar inelastic deformations (a granular shear band and a granular material under simple shear), has not been made. Local rearrangements in granular materials heavily influence

their mechanical behaviour and are linked to the micromechanics. We perform a local rearrangement analysis of a shear band in Ottawa sand under triaxial compression imaged in an experimental device developed at Johns Hopkins University [8]. We then perform the rearrangement analysis for a DEM simulation of a granular material under simple shear, intended to be an equivalent representation of the Ottawa sand shear band. We compare the local rearrangement characteristics of these two deformations and evaluate whether local rearrangements in the simulated simple shear deformation are representative of local rearrangements in the shear band. We observe no striking similarity of the local rearrangement characteristics and on average, the shear band experiences greater local rearrangement. In both deformations, we notice that regions rearranging the most contribute significantly to the macroscopic strain [6]. We also observe a significant local shear and local volumetric strain coupling in both deformations.

Primary Reader and Advisor: Prof. Ryan C. Hurley.

Secondary Reader: Prof. Jaafar El-Awady.

Acknowledgements

I would like to earnestly thank my advisor, Ryan Hurley for the plethora of lessons I have learnt from him in a very short period of time. His constant and unwavering support for the entirety of my time at Johns Hopkins University has kept me motivated throughout my master's program. His patience with me and all of my shortcomings have strongly helped me learn from my mistakes. I would like to thank Dr. Ghassan Shahin for all of his suggestions and for helping me understand the experiments he performed, the output of which I analysed for my thesis. I would like to thank Dr. Chongpu Zhai, a former postdoctoral scholar at the Hurley research group for his guidance and his suggestions. I would also like to thank the graduate students in the Hurley group: Adyota Gupta, Kwangmin Lee, Brett Kuwik and Sohanjit Ghosh for all their suggestions and the lively discussions I had with them to deal with the issues I faced during my thesis. I would also like to thank Professor Jaafar El-Awady for taking the time to be a second reader for my thesis. Finally, I would like thank my parents for all the support that they have provided me with, without which I would not be at Johns Hopkins University.

Contents

List of Tables

List of Figures

Chapter 1

Introduction

1.1 Granular materials

Granular materials are a class of amorphous materials that consist of a collection of discrete particles with size no less than 1 μm. Sand, food grains, and medical pills are some examples. Given their ubiquity in nature (sand, soil) as well as their abundance in industry (medical pills in pharmaceutical transport or food grains such as rice), their mechanical behaviour is of great interest. The mechanical behaviour of granular materials is strongly dictated by the inter-particle interactions between the constituent particles. These inter-particle interactions are usually non-linear in nature. Thus, despite their abundance, the mechanical behaviour of granular materials is complex and not as well understood as the behaviour of fluids. The mechanical behaviour of granular materials is usually studied across three length scales. The first and the smallest is the micro-scale, also called the grain scale where the inter-particle interactions, forces and force chains are studied. The second is the meso-scale where the behaviour of a collection of a few grains, such as their frictional behaviour is

studied and several homogenization techniques are also used such as Eshelby theory [11]. Shear transformation zone (STZ) theory [6] is one theory (among others [12, 13]) used to link local rearrangements to the macroscopic behaviour. Finally, at the macro-scale, continuum modeling techniques similar to those used for fluids and solids are used. When a granular material is acted upon by any force in any direction of sufficient magnitude, some or all of the individual constituent particles are displaced or rearrange locally. These micro-scale local rearrangements are very influential in effecting the macroscopic behaviour and are primal to understanding the mechanics of granular materials. Since local rearrangements collectively contribute to the macroscopic behaviour [6], different local rearrangement measures are defined to help us understand and describe the mechanical behaviour of granular materials. The plastic behaviour of materials and the onset of plasticity has always been an area of great research interest given how it represents permanent deformation. Granular materials are no exception in that respect. There have been several studies experimental, theoretical and numerical [10, 1, 6] of plasticity in granular materials. A shear band that develops in deviatorically loaded sand or any other granular material is one case of a plastically deformed granular material. Experimental studies attempting to capture the mechanics of this plastic shear band deformation have evolved in their capabilities over the decades [1, 2, 14]. On the other hand, a granular material sheared by two parallel plates under plane shear flow at steady state is also a case of plastic deformation of a granular material, because removal of shear does not lead to the granular material reverting back to its initial fabric. Several micromechanical studies of granular materials under simple shear have also been made [7, 15]. A shear band by its very nature is a region of intense shear strain. The stated examples are of two (seemingly) similar deformations: first, a steady state granular

shear band nearing or at full development and second, a granular material under simple shear that has achieved steady state. While the micromechanics for these two deformations have been extensively studied separately, a direct comparison of the micromechanics of these two deformations has not yet been made.

1.2 Shear bands

A shear band is a narrow, local region of high shear strain that develops in a material when it is subjected to deviatoric loading. Although shear bands are not usually observed in brittle materials like glass at room temperature, they are observed in a broad range of other materials such as metals, ceramics, polymers and granular materials. Because the formation of shear bands precedes or coincides with failure in a material, and continued deformation of a shear band occurs at a material's critical state, understanding the mechanics inside a shear band is key to understanding failure in materials. Consequently, shear bands are also of great interest. Just as shear bands have been studied in metals and ceramics [16], shear bands and their formation in granular materials have also been studied. Figure 1.1 shows an illustration of localized deformation and shear band formation in a metallic glass [7]. The deformation of the metallic glass and the subsequent shear band formation is simulated using a finite element implementation in ABAQUS.

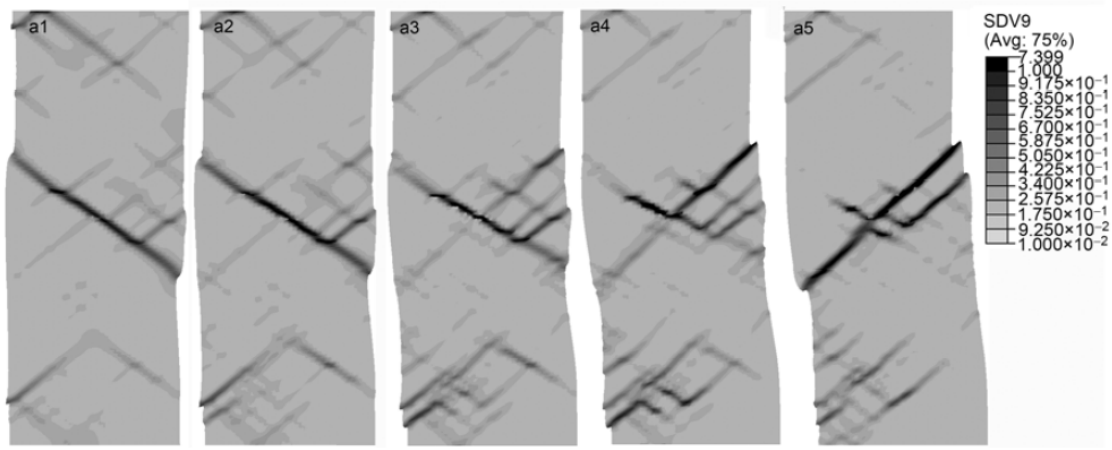

Figure 1.1: Illustration of localized deformation and shear band formation in a metallic glass under compressive loading [7]. The metallic glass sample being continuously and deviatorically loaded is simulated using a finite element implementation in ABAQUS and a map of the plastic strain field as indicated by the greyscale bar is shown. (Figure from [7]).

1.2.1 Shear bands in granular materials

The study of shear banding in granular materials such as sand has been an active area of research in geomechanics for decades. We briefly describe some influential studies conducted to capture the formation of shear bands in sand and study their mechanics. Experiments have been performed on sand in Grenoble, France for over three decades to measure deformations and characterize strain fields before, during and after the formation of the shear band. These experiments have been summarized by Jacques Desrues and Gioacchino Viggiani in their 2004 study [14]. In these experiments, a careful and systematic analysis of photographs taken of the deforming sand specimen allowed measuring deformations to predict patterns of strain localization. Stereophotogrammetry-based techniques [14] were used to photographically observe strain localization. In the 1980s, X-ray tomography was first used by Jacques

Desrues and coworkers to observe deformation and measure strain fields in shear banding sand. X-ray tomography would prove to be a very influential technique that could be used to capture grain-scale characteristics as we will describe in some of the experimental studies conducted recently.

Building on the efforts and studies conducted until 2004 to capture shear bands [14], a study conducted in 2010 [2] was the first to combine X-ray micro computed tomography (μCT) with volumetric digital image correlation (DIC) to observe and quantify the onset and evolution of a shear band in sand with grain-scale resolution. X-ray μCT and digital image correlation (DIC) were used separately in the past to study shear banding, but this was the first time they were combined to obtain the evolving displacement and strain fields at the grain-scale in deforming sand. Prior to this, micromechanical studies were confined either to 2D or artificial granular materials such as glass beads. This 2010 study [2] which was conducted for triaxially compressed sand (Hostun sand), has allowed the development of a localized shear band to be characterised. The curve in Figure 1.2 shows the Hostun sand sample's stress-strain response. We see the evolution of the deviatoric stress with axial strain when Hostun sand is triaxially compressed under a confining pressure of 100 KPa. We see the response for the different increments 1-2, 2-3, 3-4, 4-5, 5-6, 6-7 of the axial strain. Incremental analysis has shown that strain localization begins before the peak stress and a diffuse wide shear band progressively becomes thinner, evolving to a shear band that is $17d_p$ wide (d_p being the average particle diameter). The incremental maps of the kinematics of the grains, like the ones shown in Figure 1.3, suggest that localization is initiated in increment 4-5 and is fully developed in 5-6. It also appeared that the shear band contained a narrow internal core of much higher strain. This study introduced the technique of using volumetric DIC in conjunction

with X-ray μCT to capture grain scale kinematics in deforming natural granular materials like sand. Individual grains could be seen and uniquely identified in 3D. The characterised grain rotation is also shown in Figure 1.3. The individual grain rotations become progressively more intense into a zone that roughly corresponds to a fully developed shear band.

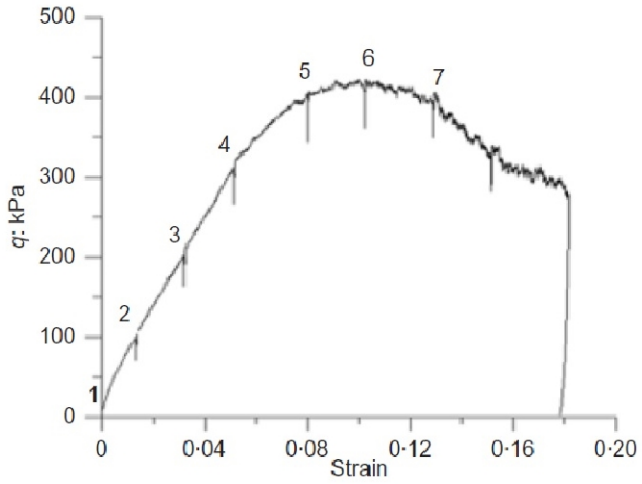

Figure 1.2: Deviatoric stress (kPa) vs axial strain for the deviatoric loading part of the triaxial compression test (for entire Hostun sand sample). We see a linear trend, followed by a curvature leading up to a peak stress at about 11 % strain followed by a plateau at which point the triaxal test was stopped. The shear band is fully developed in increment 5-6 [2]. (Figure from [2]).

Following the precedent set by studies like the previously described 2010 study [2], many studies were conducted using X-ray μCT imaging to observe and characterise grain scale kinematics [1, 4].

A recent development in geomechanics has been the increasing focus on small scale mechanisms contributing to the macroscopic behaviour [17]. In sand, for example, recent in-situ experiments combined with imaging capabilities of modern X-ray computed micro tomography instruments reveal small scale phenomena such as shear strain localisation. It was observed that these strain localizations occur in

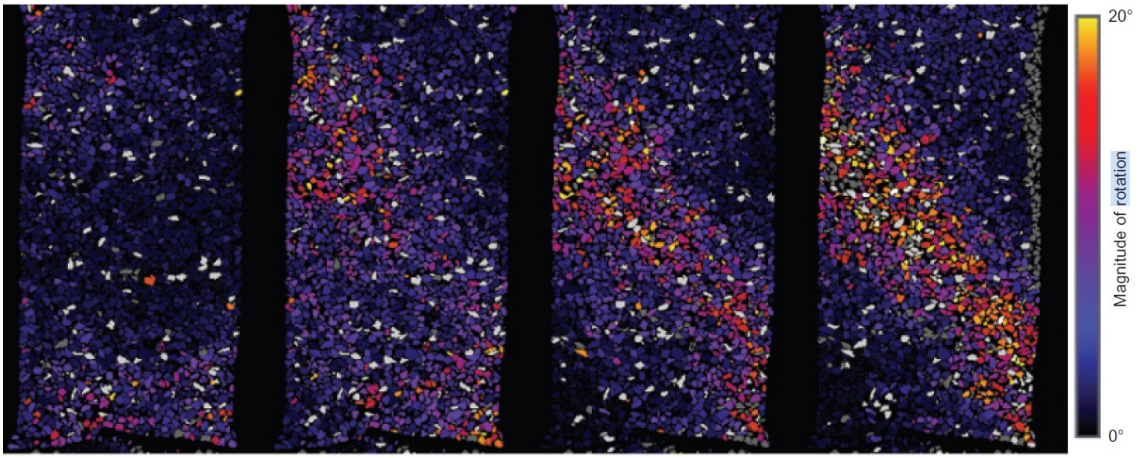

Figure 1.3: Discrete volumetric-DIC derived incremental grain rotations (magnitude) for steps 3-4, 4-5, 5-6 and 6-7 of triaxial compression of Hostun sand under 100 KPa confining pressure [2]. We see that the grain rotations intensify into a zone that roughly corresponds to the shear band. (Figure from [2]).

length scales that are as long as tens of grains. This further underscores the need for increased focus in grain scale micromechanics of granular materials. What has made possible the direct observation of the mechanics of deformation on these small scales is the use of X-ray computed micro tomography imaging techniques [2] and efficient particle tracking or digital image correlation algorithms. A study conducted in 2012 [1] introduced a particle tracking approach to better capture the grain scale kinematics of deforming sand. This particle-tracking approach was tested on two different experiments. The first was triaxial compression of Hostun sand and the other was triaxial compression of rounded Caicos Ooids. Figure 1.4 shows the evolution of deviatoric stress with axial strain in these two experiments conducted at Grenoble, France [1, 14]. The macroscopic deviatoric stress vs axial strain response curve tells us that steady state is essentially achieved after the peak deviatoric stress, and the shear band is fully developed. After this, the curve plateaus.

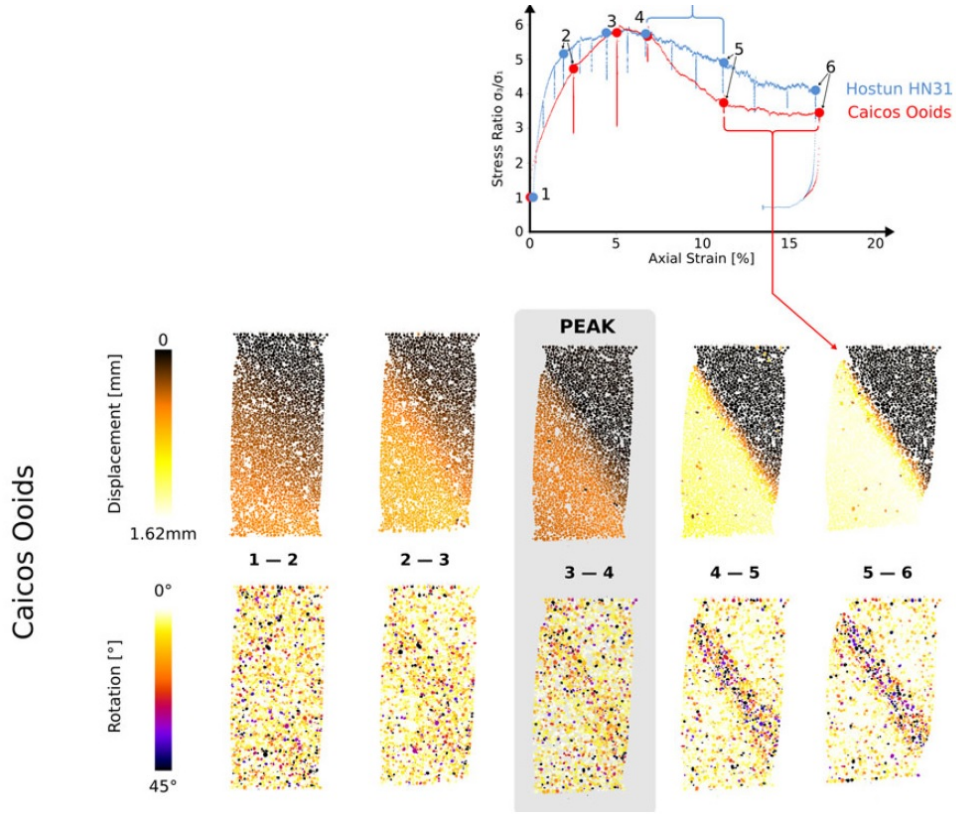

Figure 1.4: Peak deviatoric stress ratio vs axial strain for two different sands (top). Illustration of shear band mechanics from incremental grain displacements and rotation obtained after X-ray μCT and DIC (bottom) of shear banding Caicos Ooids [1].We see the grain scale displacements and rotations for steps 1-2, 2-3, 3-4, 4-5, 5-6. Peak deviatoric stress occurs at 3-4 when the shear band is fully formed. (Figure from [1]).

The bottom section of Figure 1.4 clearly demonstrates localized deformation and shear band formation in triaxially compressed Caoicos Ooids [1]. We see again in Figure 1.4, that the deviatoric stress vs axial strain response is similar to the one in the 2010 study [2] (Figure 1.2) described earlier. The shear band starts to develop before peak deviatoric stress and is wide and progressively becomes thinner and fully developed at and after peak deviatoric stress, following which the curve plateaus. Another observation was that the width of the fully developed shear band and the

strain at the peak deviatoric stress is different for Hostun sand and Ciacos Ooids. For example, in this 2012 study, the width of the shear band in deforming Caicos Ooids sand was found to be about $7d_p$, where d_p is the average particle diameter (the width of the shear band can also be measured using DIC). However, in the 2010 study described previously, the width of the shear band in Hostun sand was found to be about $17d_p$. This difference was attributed to the differences in the grain size and morphology, although further exploration is needed [1].

Another recent experimental study of shear bands conducted in 2015 [4] involved several triaxial compression tests on sands at different confining pressures. Triaxial tests were performed on Ottawa sand and Hostun sand at different pressures up to 7000 KPa. In these studies, grain breakage was also captured and analysed. The deviatoric stress and volumetric strain vs axial strain curves at different confining pressures obtained from the triaxial compression study [4] are shown in Figure 1.5.

We see a progressive reduction in the peak deviatoric stress to mean stress ratio (or q/p ratio) as well as an increase in the peak deviatoric stress value with increasing confinement pressures. The difference between the peak deviatoric stress and the plateau is large at low confining pressures, which also reduces with increasing pressure, as does the normalized q/p ratio. The considerable dilation that Ottawa sand undergoes at lower pressures also progressively reduces with increasing pressure.

All three studies described above underscore the recurring characteristics of the mechanical response of shear banding sand, one which involves the onset of development of the shear band before peak deviatoric stress, followed by a plateau, at which point the shear band is fully developed. As the peak deviatoric stress is approached, the width of the shear band also reduces until the shear band is fully developed, after which the width of the shear band is constant. These recent strides in experimental

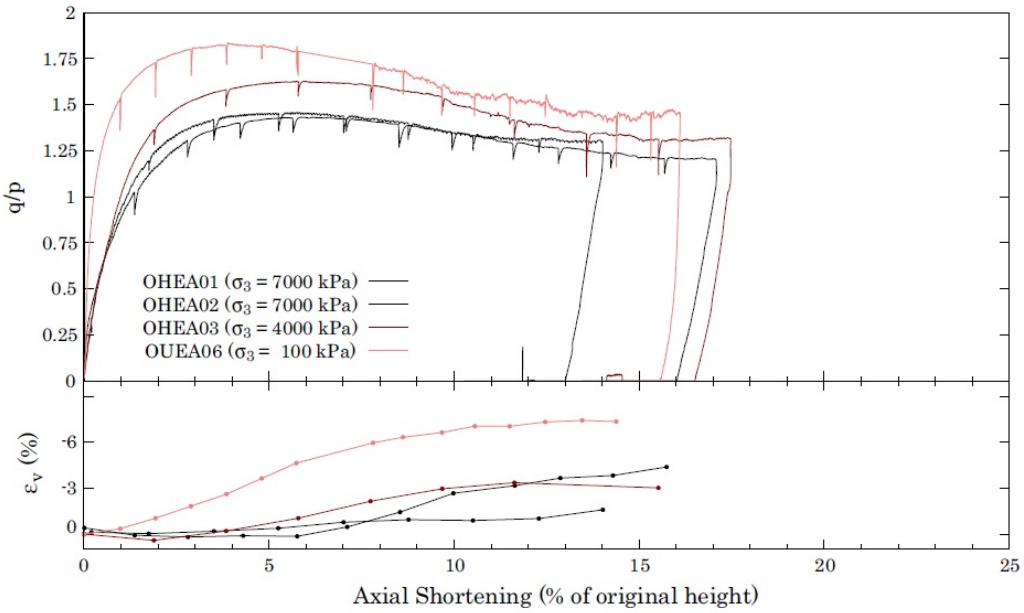

Figure 1.5: Deviatoric stress normalised by mean stress vs axial shortening and volumetric strain vs axial shortening for triaxial compression tests on Ottawa sand [4]. (Figure from [4]).

techniques involving X-ray computed tomography imaging capabilities and efficient DIC with particle tracking algorithms have significantly helped reveal the mechanics of shear bands at high spatial resolutions. These deformation measurements yield the particle centroid positions, the particle radii and the particle displacements. These quantities are sufficient for calculating the strains and quantifying the local rearrangements (which we will describe in detail in Chapter 4). Using these deformation measurements of a shear band to conduct a local rearrangement analysis has not been done before.

We have described some recent experimental studies of shear bands. On the other hand, in the granular flow community, many studies of granular materials under simple shear are conducted [18, 19, 20] to study their critical state behaviour and

transition. Here we study a case of an inelastic deformation in granular materials that is similar to an almost-fully-formed steady state granular shear band. Shear bands alone have been studied extensively and several studies describing granular materials under simple shear have also been studied. However, a connection between these two plastic deformations has not been made, which we attempt to make in this thesis.

With the computational capabilities of modern computers, and with easy access to a plethora of softwares, performing a simulation of a granular material under any condition is no longer a tedious task. While granular materials are still relatively poorly understood, several models have been proposed in the past two decades to understand their flow [20]. The shear flow of granular materials across flow regimes has been a particular focus of many of the models proposed. The portion of the granular material in a shear band is under a state of intense shear strain. Hence, we believe it is worthwhile exploring whether the knowledge we have about granular materials under simple shear can give us any insight into a granular shear band. We look for any similarities between a granular shear band and a granular material under simple shear and we do so using the lens of local rearrangements. We compare the local rearrangements and also quantify the contributions of these local rearrangements to the macroscopic strains that the granular samples experience [6].

1.3 Overview of thesis

As described in the last few paragraphs of the previous section, our motivation is to make a direct comparison of the micromechanics and local rearrangements of two similar deformations: first, a fully formed, experimentally generated shear band in

Ottawa sand; second, a simulation of a granular material under going simple shear. We extract two equivalent strain snapshots of these two deformations. The first is of shear banding Ottawa sand between two load steps. The other is of the simple shear simulation between two timesteps with strain that matches that of the shear band. We compare the local rearrangements of these two strain snapshots.

In Chapter 2, we briefly describe the triaxial compression experiment performed on Ottawa sand. This experiment was performed using an apparatus named HP-TACO [8], designed and built at Johns Hopkins University. Members of the Hurley research group performed the experiment at a high confining pressure of 10 MPa, which has not been done previously. We primarily discuss the outputs of the experiment relevant to our efforts to study the local rearrangements in the sample and the shear band. In Chapter 3, we discuss a simple shear DEM simulation we performed to compare with the experimental output obtained in Chapter 2. In Chapter 4, we discuss the methodology followed to calculate the strains and quantify the different local rearrangement measures for both the experiment and the equivalent DEM simulation. In Chapter 5, we present our results and compare the local rearrangements, their cross correlations and contributions to macroscopic shear strain for the experiment and the equivalent DEM simulation. Finally, in Chapter 6 we discuss our conclusions from the results we have obtained and we briefly describe what work we wish to explore in the future.

Chapter 2

Shear band generation during triaxial compression of Ottawa sand

An experimental triaxial compression device called a High Pressure TriAxial COmpression instrument, which we refer to by its acronym (HP-TACO) was developed at Johns Hopkins University [8]. This device is used to compress a sample of Ottawa sand using an actuator and a load cell while it is confined by a membrane. The membrane is surrounded by water maintained at a confining pressure of 10 MPa using a pump. A schematic of the setup is shown in Figure 2.1(a). The actuator allows us to impose an axial strain. The load cell facilitates measurement of the stress response.

The sample is compressed and eventually a shear band is formed and we wait until steady state is achieved and the shear band is fully developed to perform our analysis. Micro computed tomography (μCT) techniques that we referred to when describing previous shear band experiments are used to obtain the scans of the sample at different load steps illustrated in Figure 2.1 (b),(c),(d). In-situ X-ray tomography was performed for every 2% of axial shortening, followed by continuum and discrete

digital image correlation (DIC).

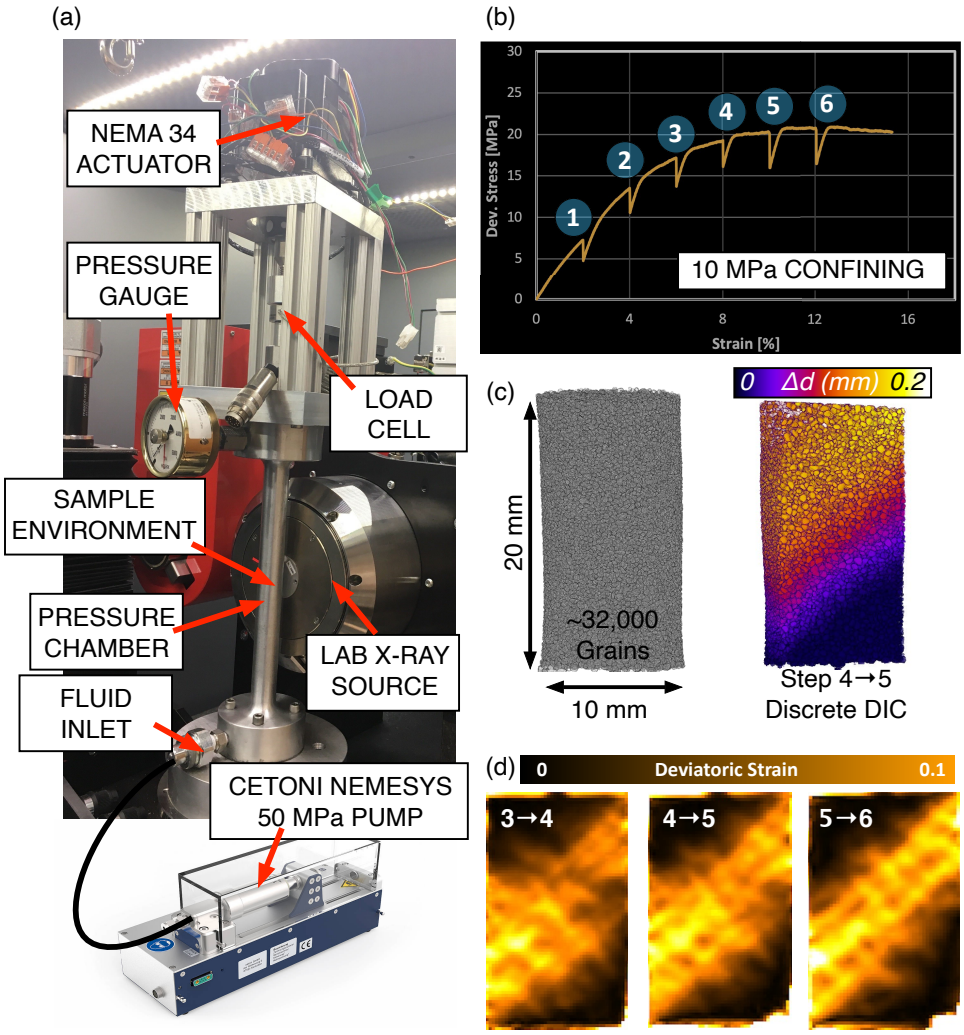

Figure 2.1: (a) HP-TACO components. (b) Deviatoric stress v/s strain at steady state. (c) Sample DIC. (d) Discernible shear band from deviatoric strain.

For each tomography image, segmentation and particle-tracking is performed in SPAM [21]. The output of segmentation and the discrete and continuum DIC is then used to obtain the particle sizes, the particle centroid positions and their displacements, which are needed to quantify the local rearrangements (description of which will come in Chapter 4). The Ottawa sand sample is polydisperse and consists

of around 32,000 grains. In Figure 2.1(b), between load steps 4 and 5, we have the positions, displacements and deformation gradients of each particle which we use to quantify the local rearrangements. As described in the studies [2] mentioned in Chapter 1, Section 1.2.1, at the peak deviatoric stress, which is what steps 4-5 correspond to, the shear band is essentially fully formed. We assume no breakage takes place and the particle size cumulative distribution is shown in Figure 2.2.

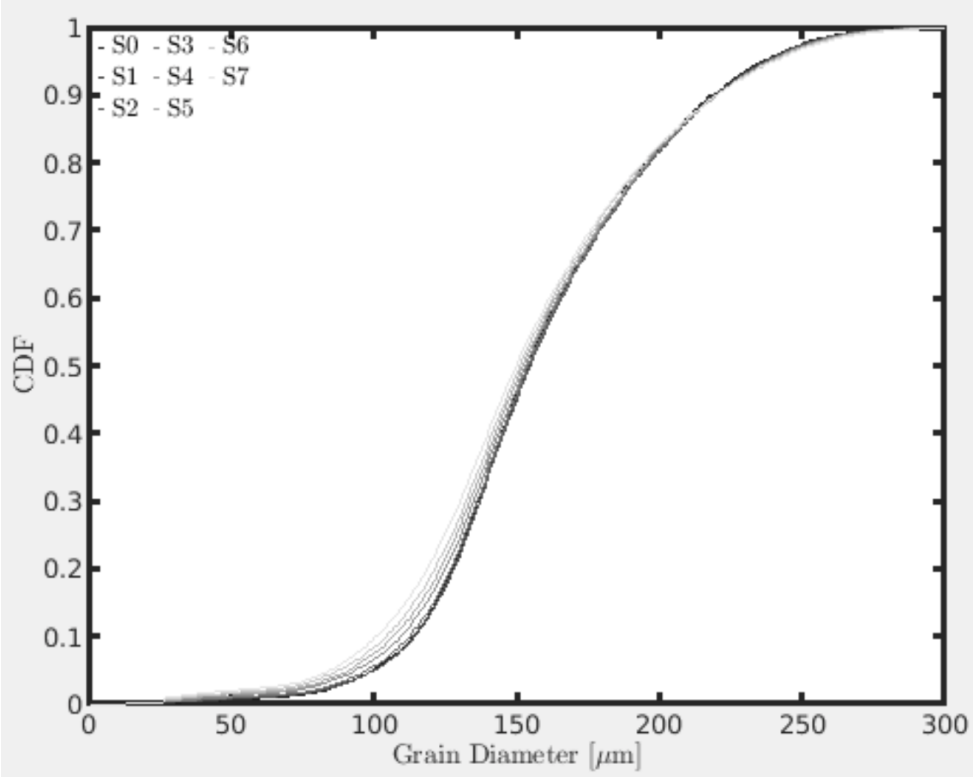

Figure 2.2: Cumulative distribution of particle sizes in the entire Ottawa sand sample.

Figures 2.1 (b) and (d), show the deviatoric stress vs strain between steps 4 and 5 (when steady state is achieved). We clearly see a discernible shear band is formed. Discrete and continuum DIC analysis performed also helped measure the size of the shear band (width), which is $10d_p$ where d_p is the average particle diameter. We

see that the deviatoric stress vs axial strain plot in Figure 2.1 (b) is similar to the ones obtained in previous triaxial sand compression experiments [4] [1] (Figures 1.2, 1.4 and 1.5). The triaxial compression experiments performed on Ottawa sand at different confining pressures were mentioned in Chapter 1, Section 1.2.1 [4]. We also noted that with increasing pressure, the deviatoric peak stress progressively gets closer to the plateau. A clear deviatoric stress peak starts to fade away at higher pressures. The highest confining pressure in the experiments conducted in the 2015 study [4] described in Chapter 1, Section 1.2.1 was 7 MPa. However, in the current HP-TACO experimental set-up, we impose a confining pressure of 10 MPa. We therefore do not see a perfectly discernible stress peak and the shear band at steps 4-5 in Figure 2.1(b) is essentially fully formed and at steady state. As mentioned previously, the HP-TACO instrument can handle much higher confining pressures than were imposed in the 2015 study [4]. Figure 2.3 shows the deviatoric stress vs axial shortening (both normalised) at different high pressures for deviatorically loaded Ottawa sand. The top right section of Figure 2.3 also shows the deformed granular sample. The Ottawa sand sample occupies a cylindrical sample volume (Figure 2.3) and is compressed from the top while being confined by a membrane that exerts a pressure of 10 MPa from the water surrounding it. The water flows to surround the membrane through a pump.

We extract a shear band after we plot a heat map of the vertical local strain component ϵ_{zz} and the local shear γ_{max} for all the grains (we describe how we calculate ϵ_{zz} and γ_{max} in Chapter 4) as illustrated in Figure 2.4. After we calculate ϵ_{zz} and γ_{max} for all the grains and plot a heat map, we see a clearly discernible shear band in Figure 2.4. To extract the shear band section, we first view the shear band along the y-axis since the shear band is predominantly in the xz plane. Then, we subjec-

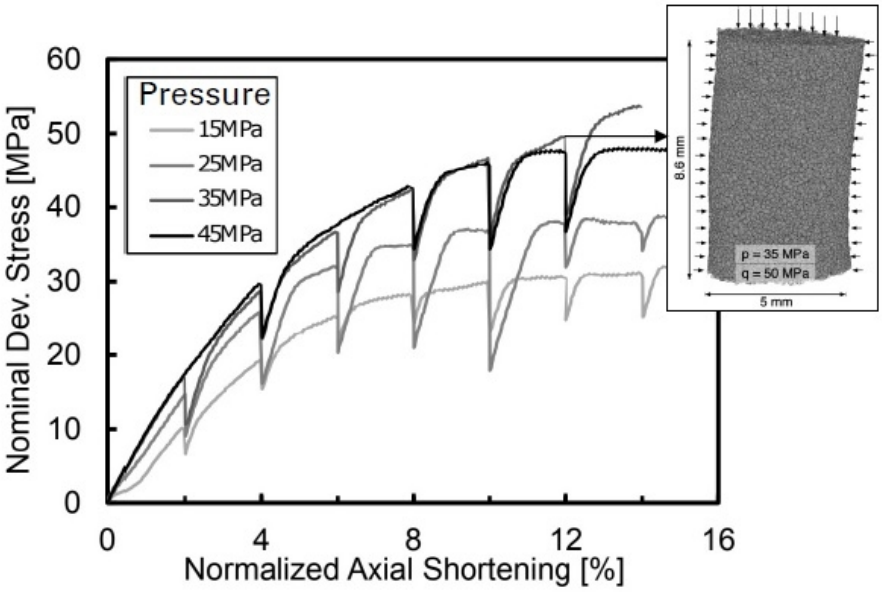

Figure 2.3: Deviatoric stress vs axial shortening in deviatorically loaded Ottawa sand at different confining pressures.

tively select two points that lie on a straight line that passes through the bottom of the shear band referred to in Figure 2.5. The slope of this xz plane line gives the angle of the shear band. Using this angle we rotate our coordinate system about the y-axis by the shear band angle. Once our coordinate system is rotated and we have the equation of the line defining the bottom of the shear band, we make use of the observation that the height of the shear band is approximately $10d_p$ and we obtain the equation of the straight line that represents the top of the shear band (since it is $10d_p$ away from the bottom line of the shear band). Both the top and bottom lines are depicted in Figures 2.5 and 2.6. Setting these two lines as the limits we can identify all the particles that lie between these two lines as those that lie inside the shear band. This shear band consists of around 8,500 particles by this method.

In this chapter, we have described the experiment performed to generate a shear

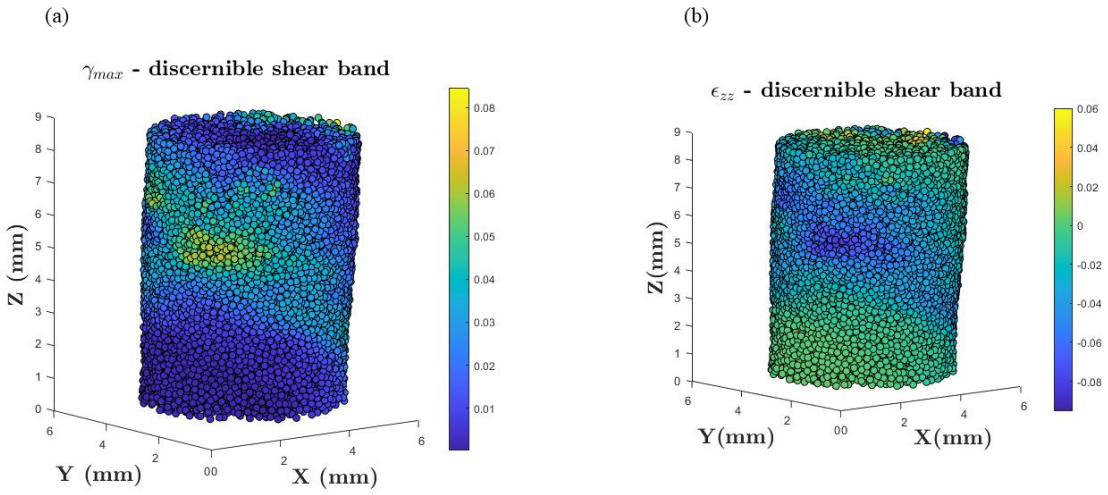

Figure 2.4: Discernible shear band from heat map plot of (a) γ_{max} and (b) ϵ_{zz}. (calculation of γ_{max} and ϵ_{zz} will be described in Chapter 4).

band in triaxially compressed Ottawa sand followed by a brief description of how the particle centroids and particle radii of the grains in the sample are obtained. We also illustrated how we extract the shear band in the sample which is our primary interest here. This is the first of the two deformations we wish to compare. In the next chapter, we describe the second deformation which is a simulation of a granular sample under simple shear. In Chapter 4, we discuss how we quantify the local rearrangements in any granular assembly and we apply the quantification methodology to both the shear band and the sample under simple shear to obtain the local rearrangements of these two deformations. In Chapter 5, we compare the local rearrangement characteristics of these two deformations.

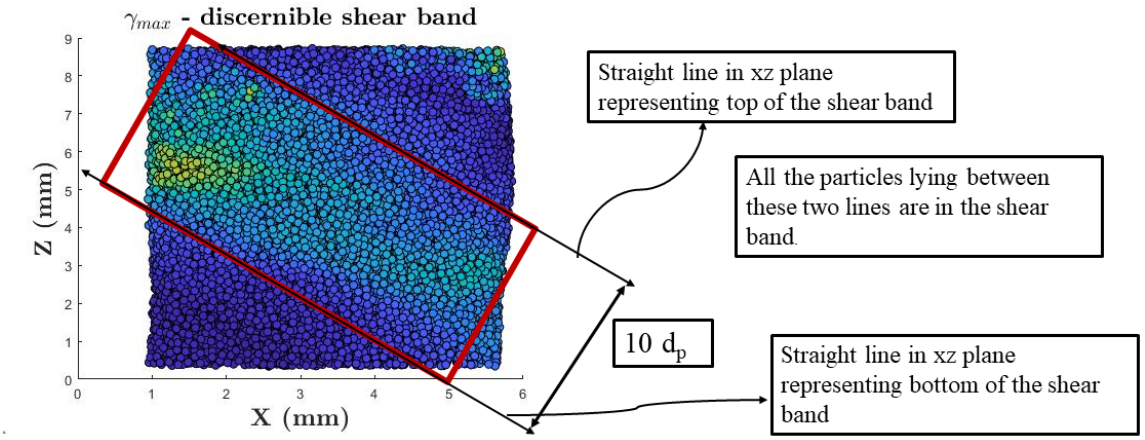

Figure 2.5: Once the shear band is clearly discernible in the xz plane, we connect two points on the bottom of the shear band. The top line is $10d_p$ away from the bottom line and parallel to it in the rotated coordinate system.

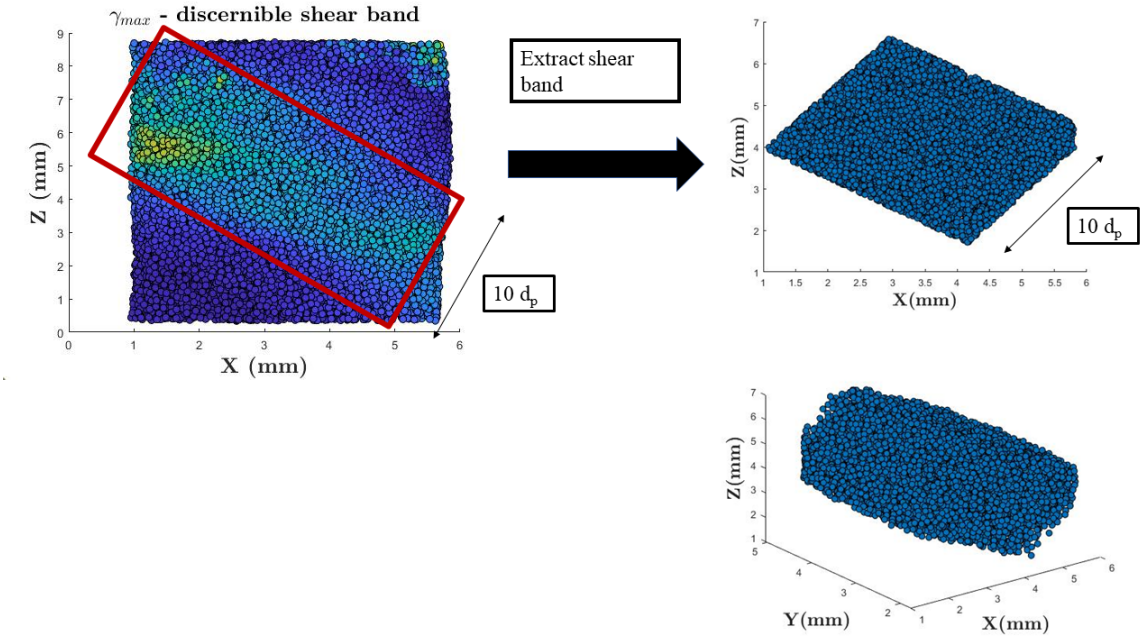

Figure 2.6: Once the shear band is clearly discernible in the xz plane and we know the equations of the two lines that represent the top and the bottom of the shear band, we can set the two lines as the limits and identify all the particles that lie between these two limits. On the top right is the xz view of the shear band. The bottom right section shows the 3D view of the angled cuboidal region that approximately constitutes the shear band. The width of the shear band as described is 10 d_p (d_p being the average particle diameter).

Chapter 3

Simple shear DEM simulation

To compare with the shear band produced from the experiment described in the previous chapter, we perform a Discrete Element Method (DEM) simulation of a granular material under simple shear. In a Discrete Element Method (DEM) simulation, based on the loading conditions, boundary conditions, inter-particle contact model and other mechanical properties such as the coefficient of friction and the coefficient of restitution, the equations of motion for each discrete particle are solved at each time instant. While this can not be done by hand, modern computers can perform these tedious calculations. We can output several per-particle properties at different times, such as the displacements, velocities, orientations, stresses, etc. We use LIGGGHTS (LAMMPS improved for general granular and granular heat transfer simulations) [22] to run the DEM simulation. We use a Hertzian contact model in our simulation and the grains are modelled as spheres. The shearing is performed by two parallel walls (both parallel to $z = 0$) and the granular sample being sheared is confined between these two walls. The particles of the granular sample are inserted in the height between these two parallel walls, in the simulation box. The walls move

in opposite directions (top wall in the negative x and bottom wall in the positive x direction) to shear the granular sample confined in between (see Figure 3.1). The other four walls that confine the granular sample are periodic in the x and y directions. We specify the dimensions for a simulation box and we also specify the density and size distribution of the particles. Based on the simulation box dimensions and the size distribution, a certain number of particles are inserted in the simulation box region. The dimensions of the simulation are the same as the shear band with the height as $10d_p$ which is the distance between the two parallel shearing walls (shown in Figure 3.1) when they are moving. The length of the two parallel walls is $12d_p$ and the width is $10d_p$ (d_p is the average particle diameter). While keeping the dimensions of the simulation box the same as that of the shear band to ensure that our simulation is the same size as the shear band, we vary the particle size distribution so that the number of particles in the simulation is the same as the number of particles in the shear band. The sample now contains 8,900 particles. After these 8.900 particles have all been inserted and settled, the two parallel walls shear this granular sample as mentioned. The walls are made up of particles that are about the same size as the particles in the granular sample. These particles that constitute the wall have positions that are rigidly fixed relative to other particles in the wall (see Figure 3.1). We construct the wall this way to ensure that when these rough walls move and shear the granular sample, the wall particles interlock with and contact the particles in the sample sufficiently to ensure that the sample is being sheared sufficiently. The bottom wall is just above the $z = 0$ plane and parallel to it. The top wall is initially at a height of $20d_p$ and parallel to the bottom wall. In LIGGGHTS, particles are inserted until a specified target (specified by the user in the input file for the simulation) is reached. This target can be a regional solid volume fraction,

the total number of particles in the region, or the total particle mass in the region. In our simulation, we define the target as a regional solid volume fraction of 0.7.

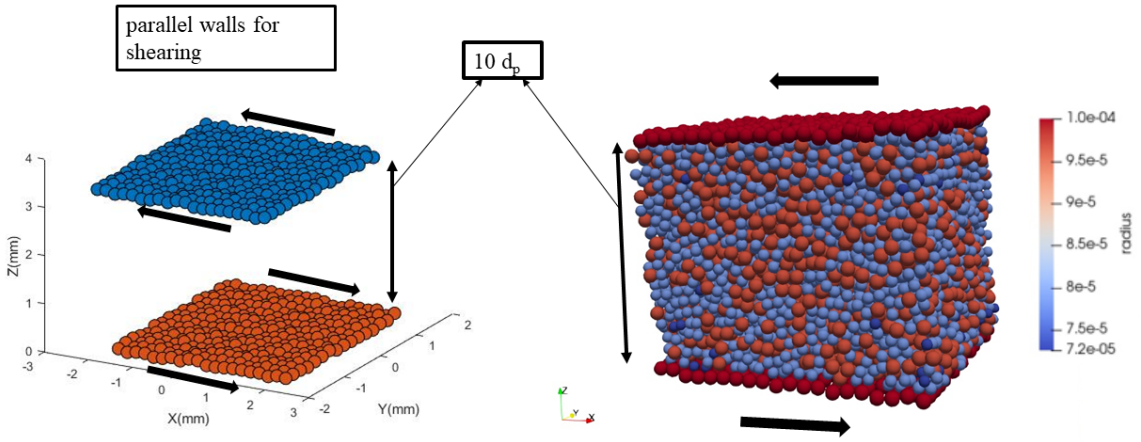

Figure 3.1: On the left are the two parallel walls that shear the granular sample. The granular sample's particles are inserted in the space between the two walls. The height between the two walls is $10d_p$, which is the same as the width of the shear band. The top wall moves in the negative x direction and the bottom wall moves in the positive x direction. On the right is a rendering of the granular sample under simple shear with the colorbar on the extreme right depicting the particle radii.

We impose a periodic boundary condition in the x and y directions mentioned previously. When we start the DEM simulation, for the first few time steps, the top wall descends until it comes into contact with the granular sample that has been inserted and compresses this sample for a few timesteps. Then, these two walls start to move in opposite directions and shear the sample. Studies [18] have shown that the parameters in the DEM simulation intended to capture quasistatic deformation must be chosen such that the dimensionless parameter known as the inertial number I lies within a quasistatic flow regime. This inertial number I is calculated as:

$$I = \dot{\gamma}\sqrt{\frac{m}{P}}, \tag{3.1}$$

where $\dot{\gamma} = \frac{2v_x}{h}$ is the shear rate (v_x is the wall velocity which is equal and opposite for two parallel walls), h is the height between the walls, m is the average mass of particles, P is the confining pressure, 10 MPa. This dimensionless number can be described as a ratio of the inertial forces to pressure forces. High values of I correspond to the fully collisional regime of kinetic theory. Low values of I correspond to the quasistatic critical state for soil mechanics which is of interest here.

To ensure that the shear flow is within the quasistatic critical state regime, studies [18] have illustrated that this dimensionless inertial number I must be below 10^{-4}. The wall velocity is chosen such that, given the particle size distribution, the inertial number I is within this regime. As mentioned before, the length of the two parallel walls is $12d_p$ and the width is $10d_p$. We impose a confining pressure of 10 MPa in the DEM simulation through the wall by making the wall impart a force that is $F = (Pressure) \times (Area)$, where the pressure is the confining pressure of 10 MPa (same as the confining pressure in the experiment); area is the area of the wall which is the $length \times width$.

Parameter	Value
Coefficient of friction μ	0.8
Velocity of top wall	-0.008 m/s
Velocity of bottom wall	0.008 m/s
Coefficient of restitution	0.7
Particle density ρ	2500 Kgm^{-3}
Time step	2x10^{-8} seconds

Table 3.1: DEM simulation parameters

We run the simulation until steady state is achieved. We dump output files after every 20,000 time steps where one single timestep is 2×10^{-8} seconds. The output file at each of these timesteps provides the positions of each particle, the particle stresses,

Particle radius in μm	Number Share in %
70 μm	25 %
72.5 μm	25 %
78 μm	25 %
97 μm	25 %

Table 3.2: Particle size distribution for DEM

the orientations, velocities and several other kinematic quantities. We observe that it requires around 10 million time steps for steady state to be achieved. The steady state velocity profile is shown in Figure 3.2. We select two points in time such that the macroscopic shear associated with the time difference of these two time steps is the same as the macroscopic shear strain of the shear band. This timestep difference can be calculated from:

$$\frac{2 \times (Wall - Velocity) \times (\Delta t) \times (timestep)}{h} = \Delta \epsilon_{xz}^{SB} \tag{3.2}$$

where h is the height which is $10 \times d_p$ and d_p is the average particle diameter. $\Delta \epsilon_{xz}^{SB}$ is the macroscopic shear strain that the entire shear band experiences between the two load steps for which we analyse experimental data (load steps 4 and 5). Also, in the local rearrangement analysis for this simple shear DEM simulation, we only consider a central flow region away from the x and y periodic boundaries to ensure the particles for which we calculate the local rearrangements do not cross the periodic boundary. Figure 3.3 shows the macroscopic response of the DEM simple shear simulation. The shear stress and the vertical stress achieve steady state with strain. The steady state shear stress is around -1.75 MPa.

In the previous chapter (Chapter 2) we described how we obtain the particle centroid positions and the particle radii of the grains in an experimentally gener-

ated shear band. In the current chapter, we have described how we obtain the per particle kinematics which includes the particle centroid positions and particle radii of a simulated granular sample under simple shear. In the next chapter (Chapter 4), we describe how we use these centroid positions and particle radii to calculate the strains and quantify the local rearrangements in both the shear band and the simulated granular sample under simple shear.

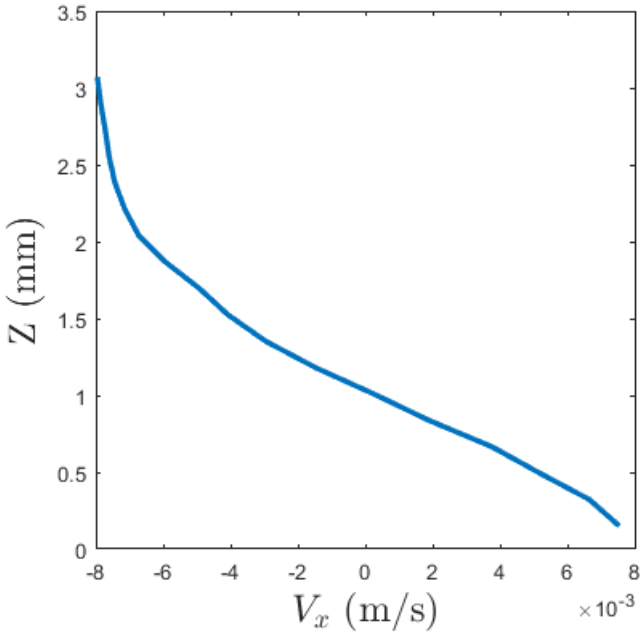

Figure 3.2: Steady state velocity profile of the granular sample under simple shear. We obtain the velocities of the particles from the output of the DEM simulation. We divide the the entire sample into several stratified layers in the z-direction. We plot the average of the x-velocity components of all the particles for each layer (each layer has a specific height z) to obtain the velocity profile.

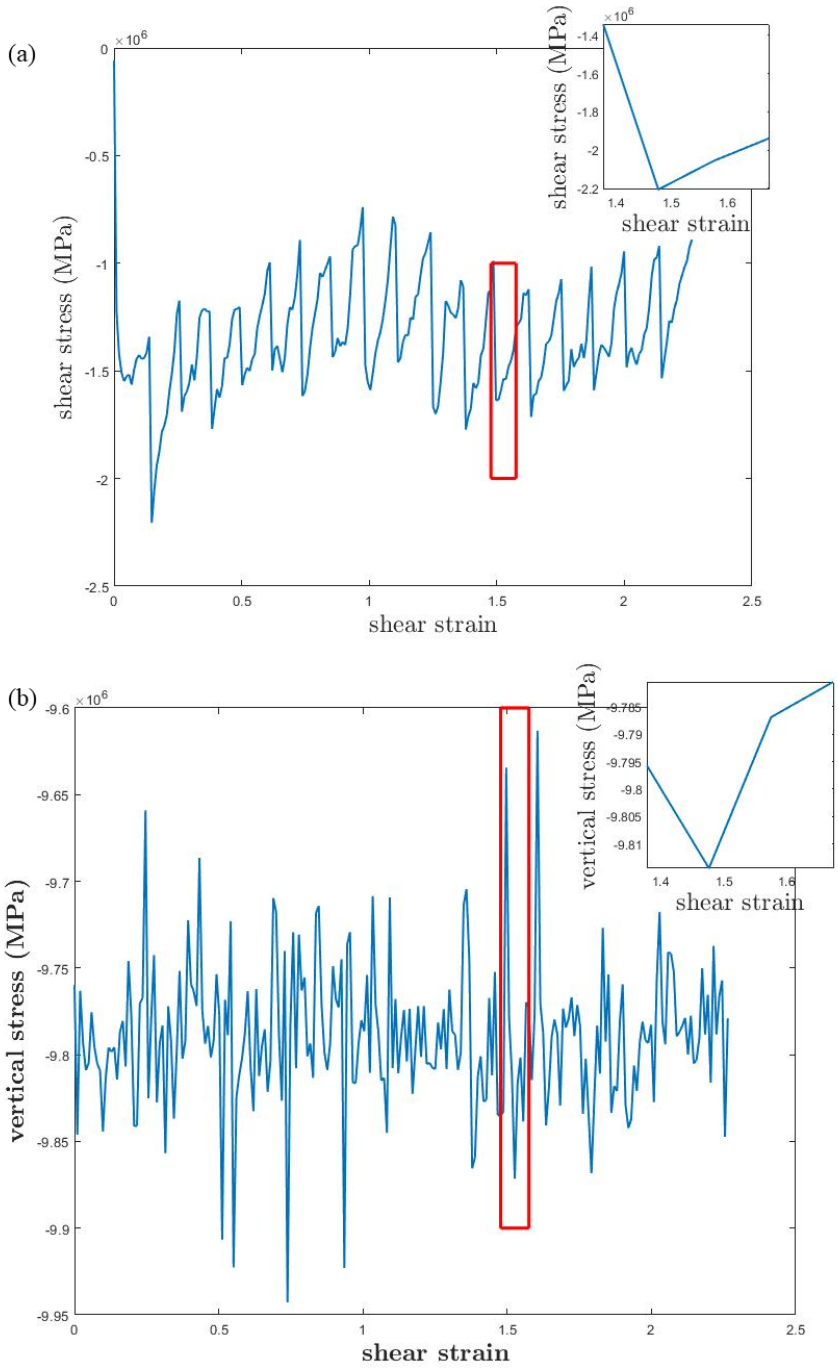

Figure 3.3: Macroscopic stress-strain response of the granular sample under simple shear. We also highlight the strain snapshot chosen such that the strain associated with this snapshot is the same as that of the shear band. (a) Macroscopic shear stress response (b) Macroscopic vertical stress response

Chapter 4

Methodology for quantifying local rearrangements

4.1 Strain calculation

In order to quantify the local rearrangements, we first need to calculate different strain measures for the entire granular assembly (whether for the experimental shear band or the simulation). To calculate the strains, we need the particle centroid positions and the particle radii at both the load steps (for the experimentally generated shear band) and both the timesteps (for the DEM simulation). The source of these particle centroid positions changes depending on whether it is for the shear band (DIC from micro CT data) or the simple shear DEM simulation (particle centroid positions are the output of the simulation at different times) [23]. After we have the particle centroid positions between the two times, the procedure to calculate the strains is the same which we describe next. We use Bagi's method to calculate strains in granular assemblies as described in [24]. To calculate the strains, we

first construct a radical Voronoi tessellation in Voro++ [25, 26] at both the times (and load steps) using the particle centroids and the particle radii, we subsequently construct the Delaunay triangulation, the dual network to the Voronoi tessellation. This Delaunay triangulation is similar to a mesh in finite element method problems consisting of several tetrahedrons (in 3D) or triangles (in 2D). The particle centroids serve as the nodes for these tetrahedrons. One caveat we wish to mention is that for the Voronoi tessellation of the Ottawa sand sample (experiment), we assume the entire sample is monodisperse with all particles having the same diameter of d_p (average particle diameter of the entire sample). We do this because the polydispersity of the Ottawa sand sample is such that some very small-sized particles are in close contact with particles that are much larger. Because of this and our chosen method of constructing tessellations using Voro++, when a tessellation is constructed, the Voronoi cell associated with the large particle pushes the small particle centroid outside of its own Voronoi cell, leading to the smaller Voronoi cells getting destroyed and fewer Voronoi cells than particles in the sample. Hence, we assume monodispersity to avoid this problem. Figure 4.1 shows the Delaunay triangulation generation for the first load step of the two analyzed from the experiment and Figure 4.2 for the first of the two timesteps from the DEM simulation. We use this initial triangulation for our strain calculations. The displacement gradient for each tetrahedron t in the Delaunay triangulation, $u^t_{i,j}$, was then calculated using:

$$u^t_{i,j} = \frac{1}{V_t} \sum_{k=1}^{4} u^k_i a^k_j. \tag{4.1}$$

V_t is the volume of each tetrahedron, k is the particle centroid forming the tetrahedron, u^k_i is the displacement of particle i at node k between load steps or timesteps,

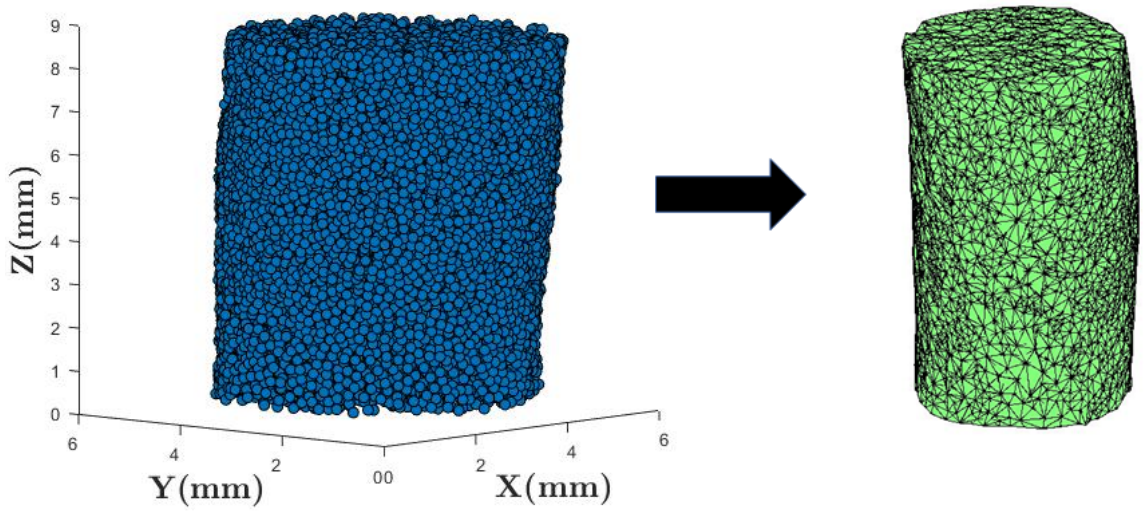

Figure 4.1: Delaunay triangulation from particle centroids. On the left we have the particle centroids of all the particles in the sample. Using the Voronoi tessellation we form the triangulation or the mesh on the right.

a_j^k is a vector with magnitude equal to the area of the tetrahedron face not containing the node k divided by space dimension (3 in 3D and 2 in 2D) pointing towards interior of tetrahedron and perpendicular to tetrahedron face not containing node k [24]. The infinitesimal strain and rotation tensors for each tetrahedron are calculated in (4.2), and (4.3) as:

$$\epsilon_{ij}^t = \frac{1}{2}(u_{i,j}^t + u_{j,i}^t), \tag{4.2}$$

$$\omega_{ij}^t = \frac{1}{2}(u_{i,j}^t - u_{j,i}^t). \tag{4.3}$$

Next, we calculate the particle centered strain for each particle using the tetrahedral strains by:

$$\epsilon_{ij}^c = \frac{1}{V_c}\sum_{t=1}^{N_t^c} \epsilon_{ij}^t V_t, \tag{4.4}$$

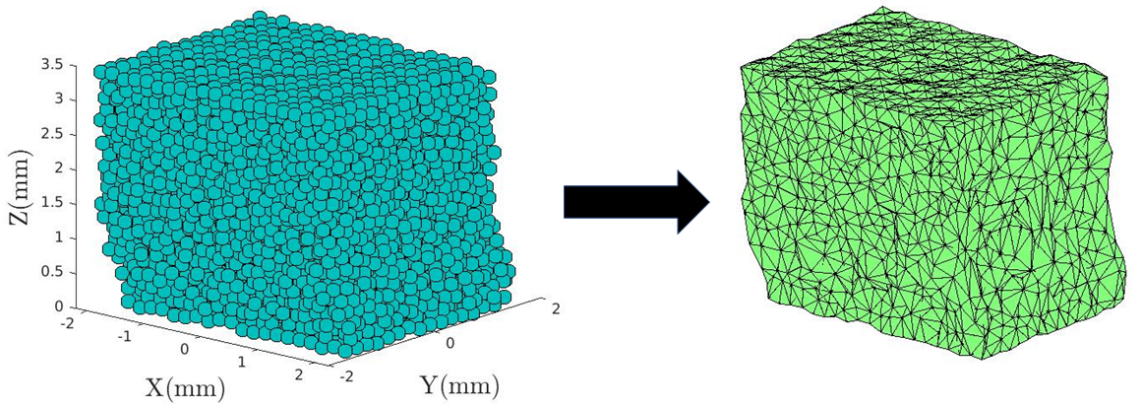

Figure 4.2: Delaunay triangulation of simple shear DEM simulation sample between two timesteps that produce the same strain as found in the shear band.

where t is the index of a tetrahedron for which a particle serves as a node, N_t^c is the number of tetrahedrons in the Delaunay triangulation for which the particle c serves as a node, V_t is the volume of tetrahedron t, ϵ_{ij}^t is the strain tensor of tetrahedron t, and $V_c = \sum_{t=1}^{N_t^c} V_t$ is the sum of the volumes of all the tetrahedrons for which contact particle c serves as a node. This is repeated for each particle in the granular sample and all the tetrahedrons in the Delaunay triangulation. With these particle centered strains, we can now compute local rearrangement measures.

4.2 Quantifying local rearrangements

Before defining and computing the local rearrangement measures, we first define a local averaging region applicable to each particle in which these local rearrangement definitions are valid. We define the local averaging region as a spherical region centered on the center of mass of the particle, of radius Nr_p, where N is an integer and r_p is the mean particle radius of all the particles in the sample. Studies conducted on local rearrangements in metallic glasses (original STZ theory paper) [6], colloidal

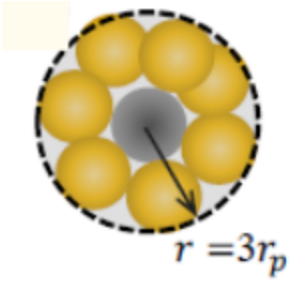

Figure 4.3: Local averaging region centered around central gray particle with its neighbours (in yellow) inside [9]. (Figure from [9]).

glasses [27] and granular materials [28] suggest that local isolated, separate and exclusive rearrangement events can be identified with D^2_{min} (a rearrangement measure which we will describe in the next few paragraphs) when the local averaging region is between $r = 2r_p$ and $r = 3r_p$. We therefore choose $r = 3r_p$ for the analysis here. We also observed that changing r between $r = 2r_p$ and $r = 3r_p$ does not qualitatively change our results significantly. Using this definition of the averaging region, we define the local strain in the averaging region corresponding to each particle by:

$$\epsilon^l_{ij} = \frac{1}{V_l} \sum_{c=1}^{N^e_p} \epsilon^c_{ij} V_c, \tag{4.5}$$

where c is the index of a particle partially or fully within the local averaging region. V_c is the volume of the particle within that region, N^c_p is the number of particles partially or fully inside the region, V_c is calculated using the sphere-sphere intersection formula [29].

We can now quantify the local rearrangement measures. We compute five metrics of local rearrangement. These metrics or measures are inspired by previous studies examining local rearrangements in metallic glasses and granular materials in the context of shear transformation zone (STZ) theory [6, 7, 30]. Three of these

local rearrangement measures, local shear (γ_{max}), dilation (ϵ_+), and contraction (ϵ_-), are based entirely on local strains defined in equation (4.5). These local measures are very important in the context of STZ theory [6, 7, 30] which assumes that the macroscopic strain is influenced almost entirely by local, isolated strain events with certain principal directions and magnitudes. One of the remaining two measures of local rearrangement quantifies non-affine particle deformation and is the well know D^2_{min} which was also first described in the original 1998 paper that proposed STZ theory [6]. The final measure is the relative particle rotation θ_{rel} which quantifies the relative rotation of a particle with respect to its neighbours in the local averaging region and the rigid body rotation of the entire granular sample as a whole. We define θ_{rel} to capture relative particle rotations known to be a signature of plasticity in cyclically sheared granular materials which may not be captured by the local strains or D^2_{min} [31, 30].

From the local strains we defined in equation (4.5), we can define the local shear, dilation and contraction in the local averaging regions as:

$$\gamma_{max} = \frac{\epsilon^l_1 - \epsilon^l_3}{2}, \tag{4.6}$$

$$\epsilon_{vol} = \epsilon^l_1 + \epsilon^l_2 + \epsilon^l_3, \tag{4.7}$$

where ϵ^l_1 , ϵ^l_2 , ϵ^l_3 are the principal strains in the local averaging region obtained from an eigen-value decomposition of ϵ^l. A local region either exhibits local dilation ($\epsilon_{vol} > 0$) in which case it is labelled ϵ_+, or it exhibits local contraction ($\epsilon_{vol} < 0$) in which case it is labelled ϵ_-.

To compute D^2_{min} for particle i between timesteps or load step s and $s+1$, we

perform the calculation in (4.8)

$$D^2_{i,min} = min \frac{1}{N^e_p} \sum_{j=1}^{N^e_p} (\Delta d^{ij}_k(s+1) - \epsilon_{kl} d^{ij}_l(s)), \tag{4.8}$$

where, $d^{ij}_k(s) = r_j(s) - r_i(s)$ is the relative position of particles i and j at time or load step s, $\Delta d^{ij}_k(s+1) = d^{ij}_k(s+1) - d^{ij}_k(s)$, ϵ_{kl} is the minimizing strain tensor, and N^j_p is the number of particles j around the central particle i in the local averaging region. Minimization is performed over ϵ_{kl}.

To calculate the relative particle rotation we first calculate the local rigid body rotation from the infinitesimal rotation for all the tetrahedrons calculated in equation (4.3) as:

$$\omega^{Ve}_{ij} = \frac{1}{V_c} \sum_{t=1}^{N^c_t} \omega^t_{i,j} V_t. \tag{4.9}$$

We use ω^{Ve}_{ij} to calculate $R^{cell}(i)$ as $R^{cell}(i) = \omega^{Ve}_{ij} + \mathbf{I}$, where $\mathbf{I}$ is the 3D identity matrix. $R^{cell}(i)^{-1} R^{xrd}(i)$ is the rigid body rotational component from $R^{xrd}(i)$ leaving only the rotation of a particle in a local frame that rotates rigidly with the material. Finally the rotation matrix describing the relative rotation of particle i relative to its neighbours j is:

$$R^{ij} = (R^{cell}(j)^{-1} R^{xrd}(j))^{-1} R^{cell}(i)^{-1} R^{xrd}(i). \tag{4.10}$$

If particles i and j rotate identically and share the same local rigid body rotation, then $R^{xrd}(i) = R^{xrd}(j)$ which when plugged into equation (4.10) yields $R^{ij}(i) = \mathbf{I}$. On other hand though, if particles rotate with respect to one another, an axis angle calculation on R^{ij} yields:

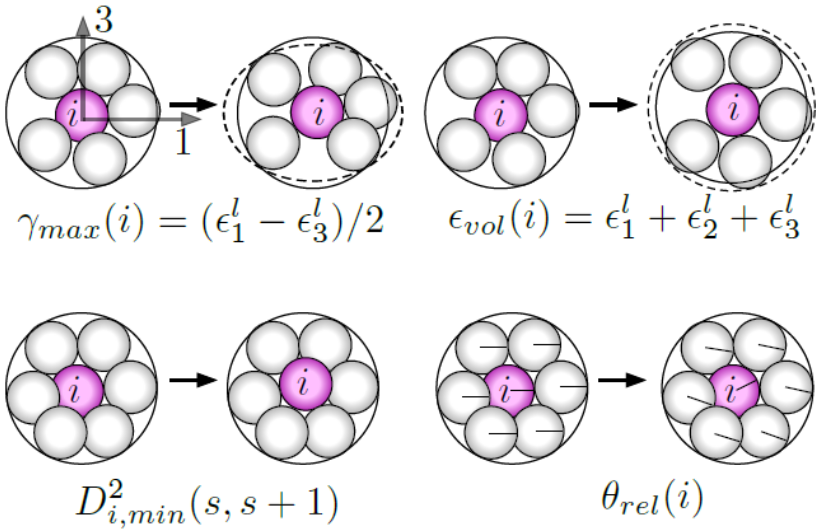

Figure 4.4: Illustration of particle rearrangements in local averaging region centered around particle i. Figure from [10].

$$\theta_{rel}(i) = \frac{1}{N_p^j} \sum_{j=1}^{N_p^j} \theta_{rel}^{ij}, \tag{4.11}$$

where N_p^j is the number of particles in the local averaging region. For the experiment, we obtain R^{xrd} from the deformation gradient, which is one of the outputs of the experiment. For the DEM simulation, R^{xrd} is obtained from the quaternions, which are in the output file from the DEM simulation.

Now that we have described how we quantify and obtain the local rearrangements in a granular assembly from the particle centroid positions and the particle radii, we can apply this methodology to both the experimental shear band described in Chapter 2 and the simulated granular sample under simple shear described in Chapter 3 to obtain the local rearrangements in both cases. We present our results in the next chapter and compare the local rearrangement characteristics of the experiment and the DEM simulation.

Chapter 5

Results: comparison of experimental shear band with simple shear DEM simulation

After completing the local rearrangement calculations for the entire Ottawa sand sample following the methodology in Chapter 4, we plot a map of the particle centered γ_{max} and ϵ_{zz} in Figure 5.1. We see a clearly discernible shear band.

From these heat maps shown in Figure 5.1, we can extract a shear band as described in Figures 2.4, 2.5 and 2.6 . From equation (3.2), once we complete the local rearrangement analysis for the shear band and we obtain $\Delta\epsilon_{xz}^{SB}$, we can obtain the equivalent timestep difference required in the DEM simulation Δt. However, when we complete the local rearrangement analysis for the DEM simulation between two time instances with timestep difference Δt, we observe that the homogenized microscopic strain between the two times is less than that of the shear band's macroscopic strain (the homogenized microscopic strain is simply the average of the local strain ϵ_{xz} component of all the particles under consideration). We posit that due to slip effects at the boundary wall, the homogenized microscopic strain does not match that of the shear band. Therefore, we choose a slightly larger time difference Δt such that the

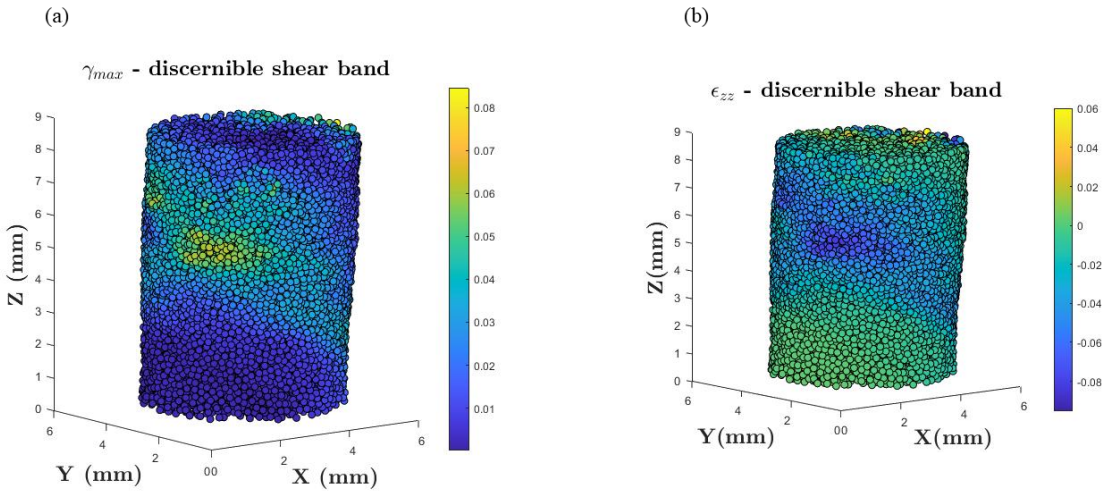

Figure 5.1: Discernible Shear Band from heat map plot of (a) γ_{max} and (b)ϵ_{zz}.

homogenized microscopic strain is the same as that of the shear band's macroscopic strain. We observe that the Δt required to produce a homogenized microscopic shear strain that matches that of the shear band is 380,000 timesteps.

5.1 Comparison of distributions of rearrangement measures

The probability distributions of the different rearrangement metrics for both the shear band and the granular sample under simple shear are shown in Figures 5.2, 5.3(a)-(b) and Figures 5.4(a)-(b). Note that the local strain tensors for all the particles in the shear band have been rotated by the shear band angle to resemble a simple shear deformation. This rotation of the local strain tensors does not affect γ_{max}, ϵ_+ or ϵ_- which are derived from the principal local strains which remain unchanged after rotation. The probability distributions of D^2_{min}, γ_{max}, and θ_{rel} indicate that there is significantly greater local shear, particle rotation and non-affine defor-

mation in the shear band than in the granular sample under simple shear. However, the probability distributions for ϵ_{vol} indicate that the granular sample under simple shear experiences greater local dilation (ϵ_+) and local contraction (ϵ_-). Hence, with the exception of local volumetric strain, the shear band generally experiences greater local rearrangement. This anomaly for local volumetric strain needs further exploration.

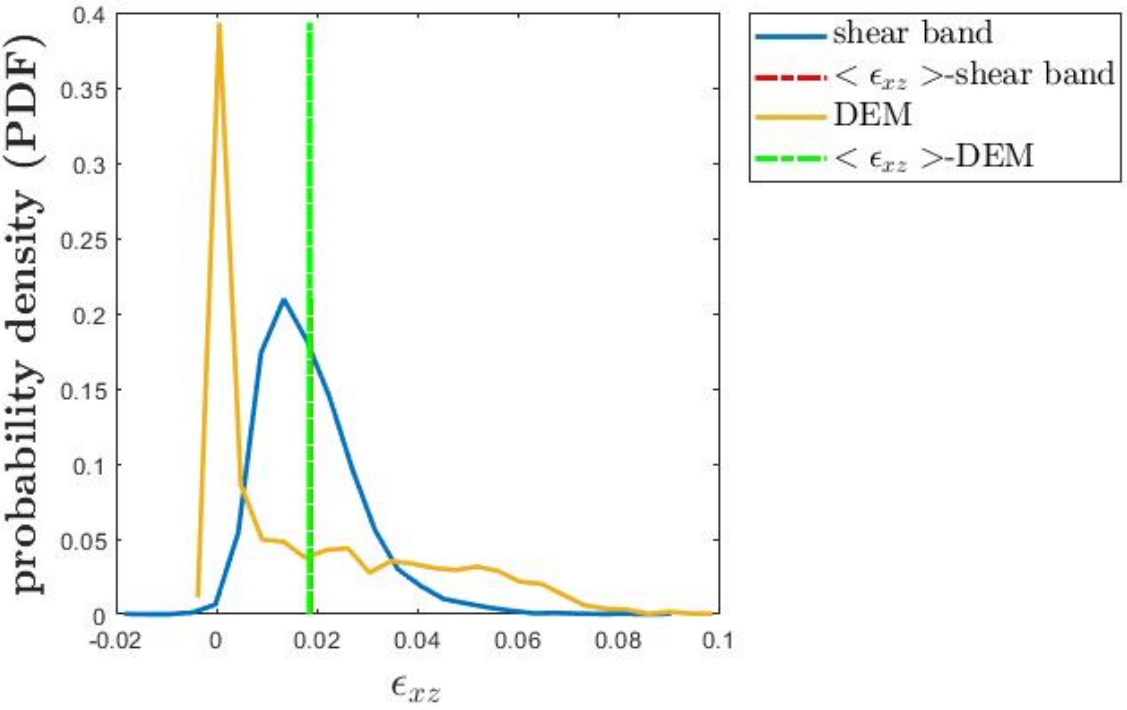

Figure 5.2: Comparison of the probability distributions of the shear strain component ϵ_{xz}. Any variable under <> denotes the average of that variable. As is evident, the average shear strain is the same for both the sample under simple shear and the shear band. Probability distributions of shear strain component ϵ_{xz} in both the sample under simple shear (yellow) and the shear band (blue) are shown.

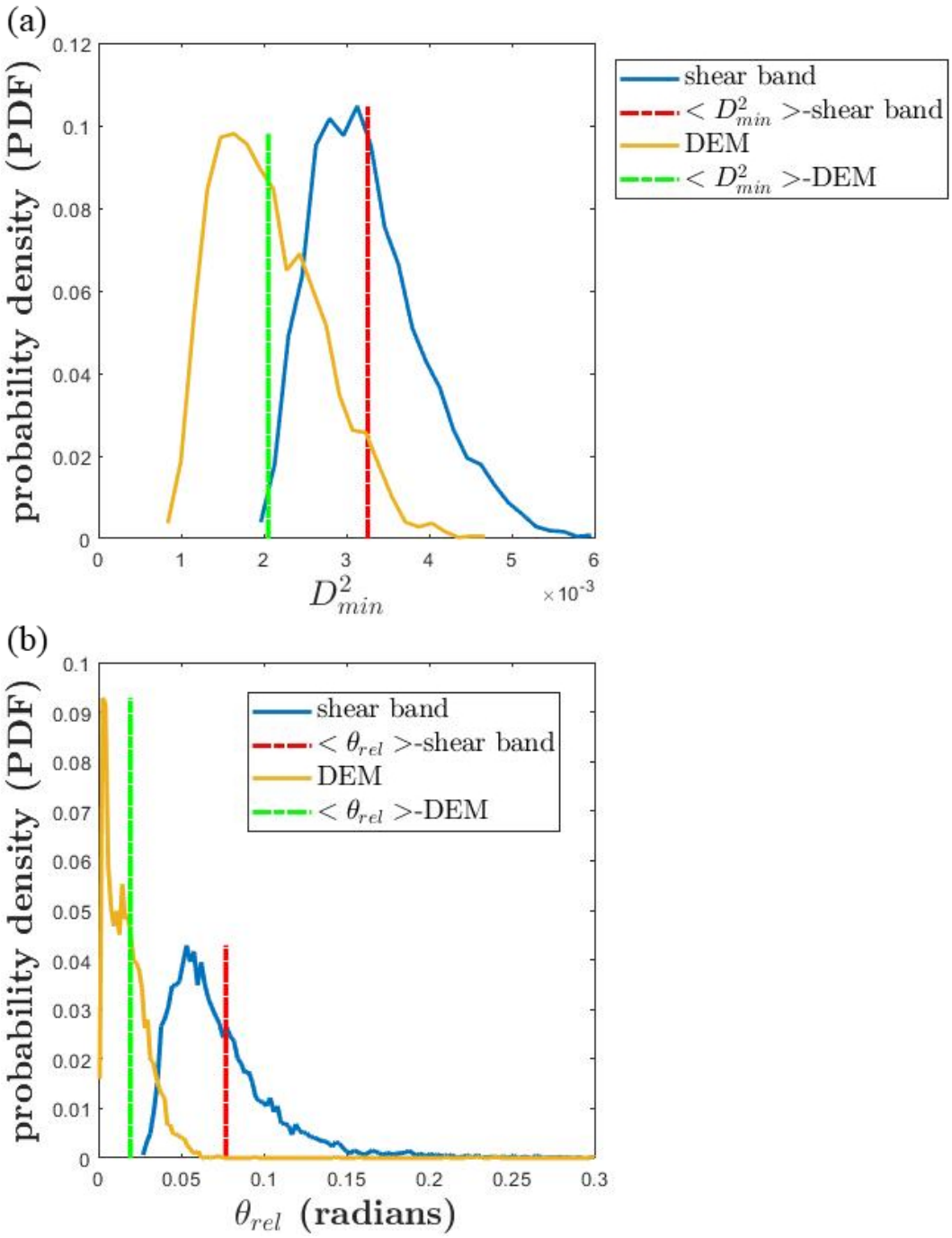

Figure 5.3: Comparison of the probability distributions of D^2_{min} and θ_{rel} in both the granular sample under simple shear and the shear band. Any variable under <> denotes the average of that variable. Probability distributions of rearrangement measures in both the sample under simple shear (yellow) and the shear band (blue) are shown for: (a) D^2_{min} (b) θ_{rel}.

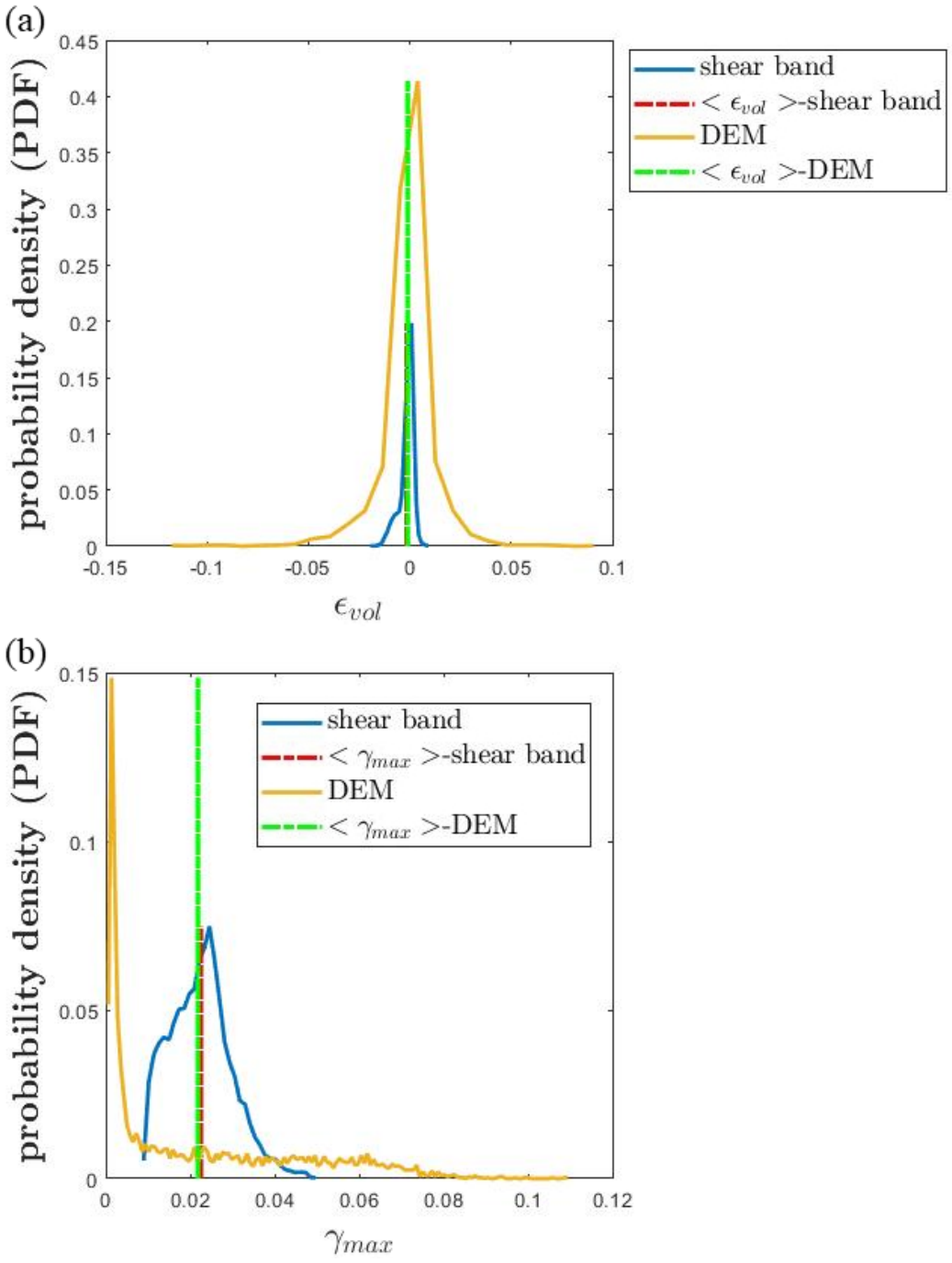

Figure 5.4: Comparison of the probability distributions of γ_{max} and ϵ_{vol} in both the granular sample under simple shear and the shear band. Any variable under $<>$ denotes the average of that variable. Probability distributions of rearrangement measures in both the sample under simple shear (yellow) and the shear band (blue) are shown for: (a) ϵ_{vol} (b) γ_{max}.

5.2 Strain contributions from rearranging regions

We calculate the fractional contribution ν to the macroscopic strain from the different local rearranging regions using the formulation [9] :

$$\nu(s, s+1, N_{\%}) = \frac{\frac{1}{V_{rr}} \sum_{i=1}^{N_{rr}} \epsilon_{xz}(i, s, s+1) V_i}{\Delta \epsilon_{xz}(s, s+1)} \tag{5.1}$$

where s is the load step (for the shear band) or the time step (DEM), $\epsilon_{xz}(i, s, s+1)$ is the particle centered strain xz component at the center of region i computed in (4.4) and V_i is the rearrangement volume ($\frac{4}{3}\pi(3r_p)^3$). V_{rr} is the sum of N_{rr} volumes V_i. $N\%$ refers to regions that experience the top $N\%$ of rearrangement by magnitude.

In Figures 5.5 (a) and (b) we calculate and observe the contributions of the regions that are rearranging the most to the macroscopic strain. We do this for the rearranging regions corresponding to each of the five rearrangement measures. For this, we first order the rearrangements by magnitude from the largest(1%) to smallest(100%), except for ϵ_- which we order from the most negative (1%) to least negative (100%). We select regions exhibiting the largest $N\%$ to $(N + 10)\%$ of rearrangement, where N varies from 0 to 90 in increments of 10. If all the regions contribute equally to the macroscopic strain or in other words, if the deformation is affine, then $\nu(s, s+1, N_{\%}) = 0.1$ or 10% for each value of N. On the other hand, if the entire deformation is furnished only by the top 10% of rearranging regions, $\nu(s, s+1, N_{\%})$=1 for $N = 0$ and $\nu(s, s+1, N_{\%})$=0 for all $N \neq 0$. We see that for both the shear band and the granular sample under simple shear, the regions that rearrange the most (regions experiencing the top $N\%$ile of rearrangements) contribute the most to the macroscopic shear strain for all five rearrangement measures. The contributions from local regions experiencing the most local shear (γ_{max}) and the most local contraction

(ϵ_-) to the macroscopic strain is higher for the sample under simple shear than for the shear band.

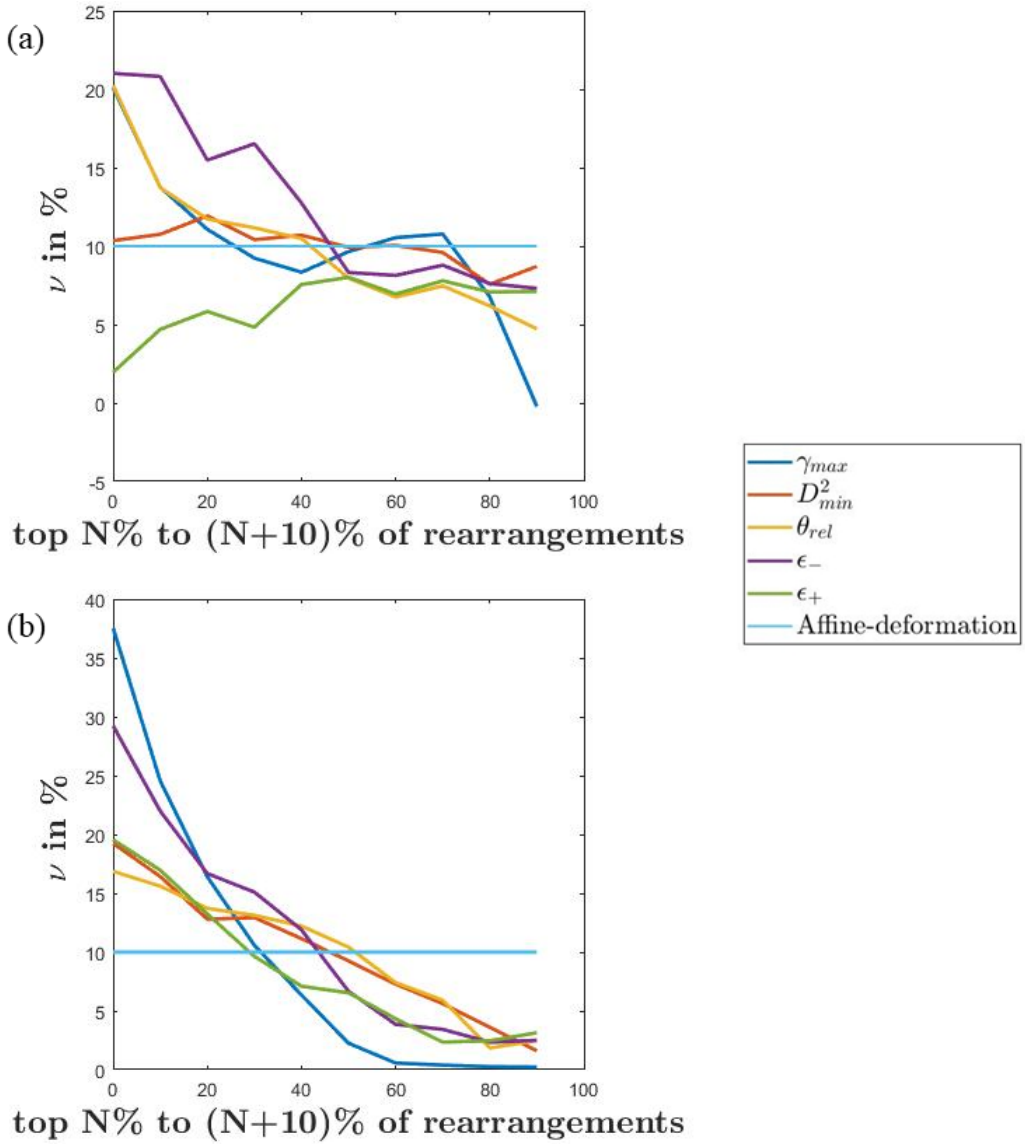

Figure 5.5: Fractional contribution in % to the macroscopic strain from the regions rearranging the most (for all the five different rearrangement measures D^2_{min},γ_{max},θ_{rel},ϵ_+,ϵ_-)(a) for the shear band (b) for the granular sample under simple shear (DEM). We select regions exhibiting the largest N% to $(N+10)$% of rearrangement, where N varies from 0 to 90 in increments of 10.

5.3 Cross-correlations between rearrangements

The cross correlations between different rearrangements in regions rearranging the most also shows some interesting results. The correlation coefficient between two rearrangement measures g and e between the same steps s and $s+1$ and in regions experiencing the top $N\%$ of rearrangements measure e can be calculated using formulation (5.2).

$$\rho_g^e = \frac{\sum_{i=1}^{N\%}[e(i,s,s+1) - < e(s,s+1) >][g(i,s,s+1) - < g(s,s+1) >]}{\sqrt{\sum_{i=1}^{N\%}[e(i,s,s+1) - < e(s,s+1) >]^2}\sqrt{\sum_{i=1}^{N\%}[g(i,s,s+1) - < g(s,s+1) >]^2}} \tag{5.2}$$

From Figures 5.6, 5.7, 5.8, 5.9, 5.10, 5.11 ((a)-(b)), we see that there is a negative correlation between γ_{max} and ϵ_{vol} in both the sample under simple shear and the shear band. This indicates that regions that shear the most locally are also contracting, which is consistent with STZ theory because shear transformation zones [6] must contract to accommodate shear when they transform. Even though the trends are similar, we observe a stronger correlation between γ_{max} and ϵ_{vol} in the shear band than in the granular sample under simple shear. In original shear transformation zone (STZ) theory [6], the strains of these shear transformation zones are aligned along the same principal axes as the macroscopic stress which restricts the coupling between shear and dilation (γ_{max} and ϵ_+). D^2_{min} and γ_{max} are more strongly correlated in rearranging regions in the granular sample under simple shear than in the shear band.

Our most notable observation (from Figures 5.7 (a)-(b), Figures 5.9 (a)-(b), Figures 5.10 (a)-(b) curves in light blue (cyan) with upward triangular symbols) is that

regions exhibiting the largest local shear strain (γ_{max}) by magnitude tend to exhibit a non-negligible correlation with the largest dilational (ϵ_+) or contractional strain (ϵ_-) and regions exhibiting the largest dilational (ϵ_+) or contractional strain (ϵ_-) exhibit non-negligible correlations with large local shear strain. Moreover, these non-negligible correlations between large local shear (γ_{max}) and large local dilational (ϵ_+) or contractional strain (ϵ_-) are stronger and more pronounced in the shear band than in the granular sample under simple shear. Similarly, regions exhibiting the largest local shear strain (γ_{max}) tend to have non-negligible correlations with the non-affine deformation (D^2_{min}) as seen in Figures 5.6 (a)-(b) and Figures 5.7 (a)-(b). We also observe that regions that contribute the most to the macroscopic strain exhibit a strong coupling between the local shear strain (γ_{max}) and the local volumetric strain (ϵ_{vol}). This coupling is much stronger in the shear band (-0.6) than in the sample under simple shear (-0.2) as is evident in Figures 5.11 (a)-(b). Similarly, we also observe coupling between non-affine deformation (D^2_{min}) and the local shear strain (γ_{max}).

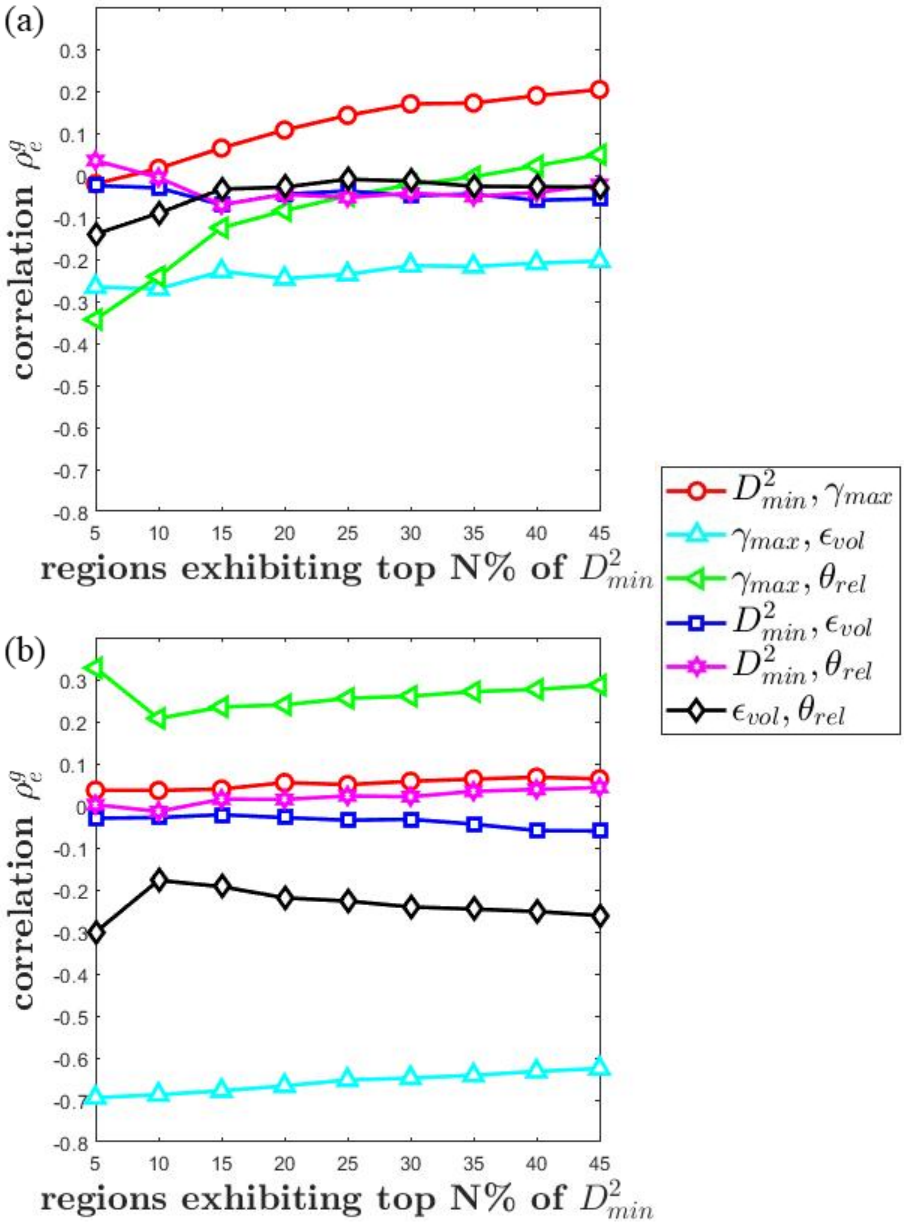

Figure 5.6: Cross-correlations between colocated rearrangements in the top $N\%$ (from largest (1%) to smallest (100%)) of all rearrangements in the shear band (bottom) and the sample under simple shear (top). Correlation coefficient between the different rearrangement measures (as calculated in (5.2)) in regions experiencing top $N\%$ (by magnitude) of (a) D^2_{min} in the sample under simple shear (b) D^2_{min} in shear band. In each case, the symbols in the legend correspond to e and g in (5.2) and N goes from 0 to 45.

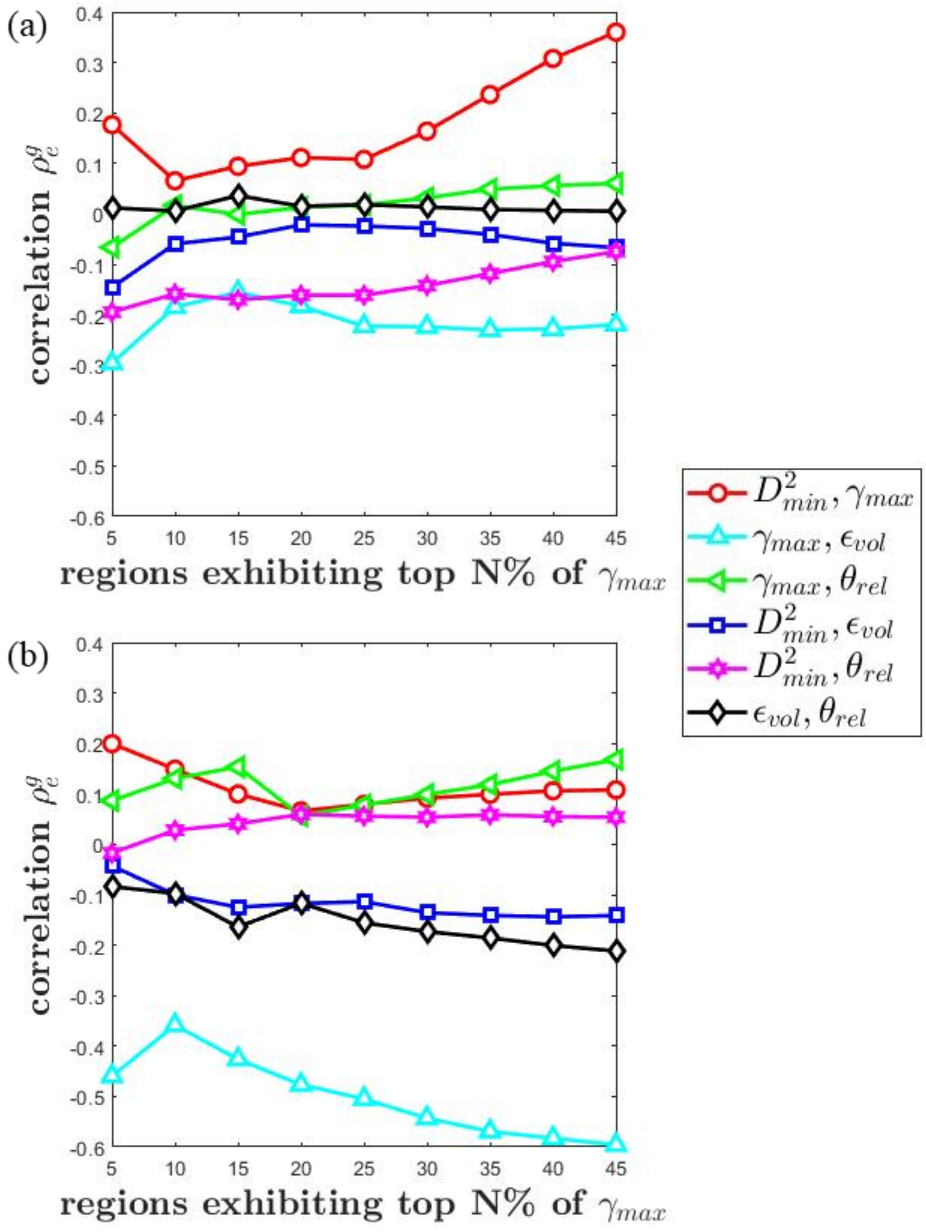

Figure 5.7: Cross-correlations between colocated rearrangements in the top $N\%$ (from largest (1%) to smallest (100%)) of all rearrangements in the shear band (bottom) and the sample under simple shear (top). Correlation coefficient between the different rearrangement measures (as calculated in (5.2)) in regions experiencing top $N\%$ (by magnitude) of (a) γ_{max} in sample under simple shear (b) γ_{max} in shear band. In each case, the symbols in the legend correspond to e and g in (5.2) and N goes from 0 to 45.

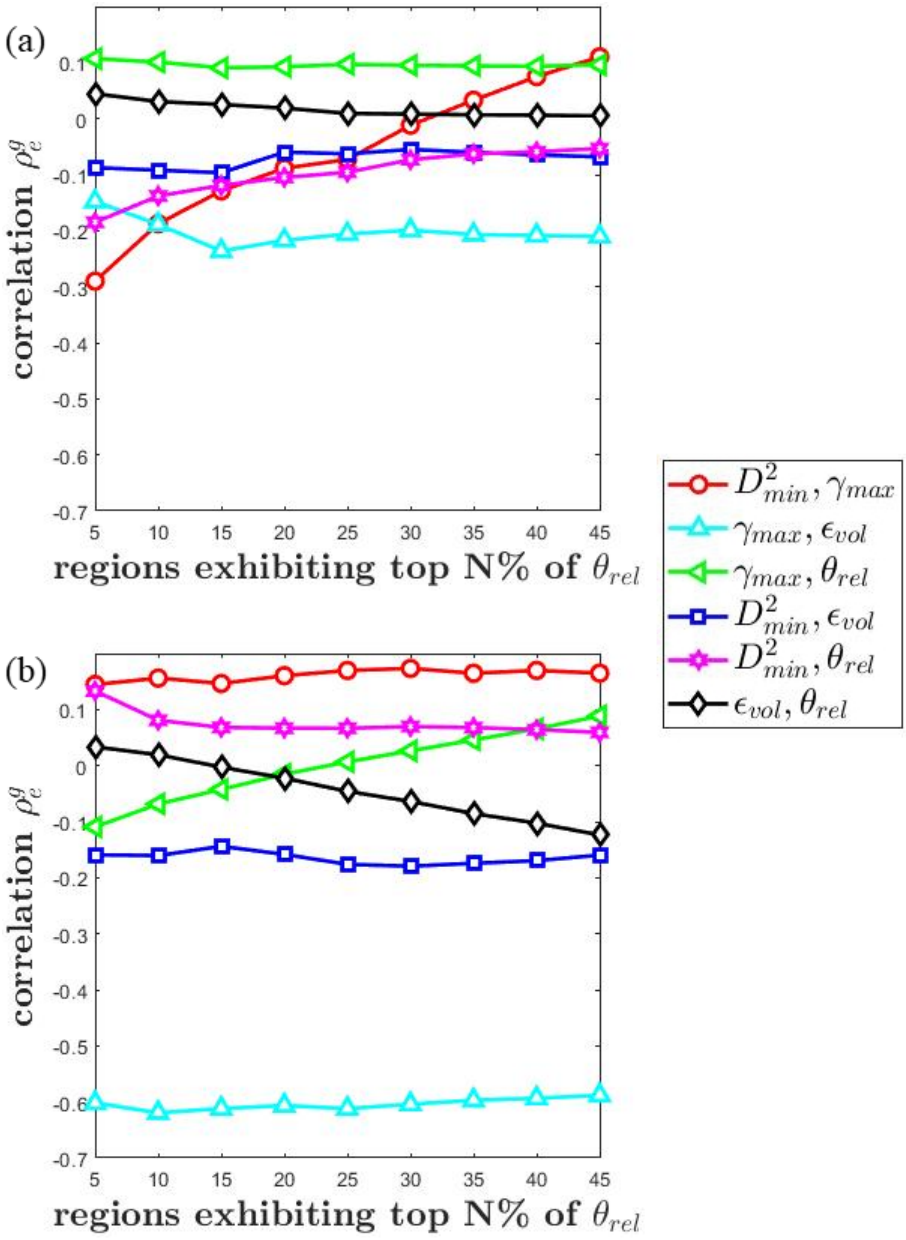

Figure 5.8: Cross-correlations between colocated rearrangements in the top $N\%$ (from largest (1%) to smallest (100%)) of all rearrangements in the shear band (bottom) and the sample under simple shear (top). Correlation coefficient between the different rearrangement measures (as calculated in (5.2)) in regions experiencing top $N\%$ (by magnitude) of (a) θ_{rel} in sample under simple shear (b) θ_{rel} in shear band. In each case, the symbols in the legend correspond to e and g in (5.2) and N goes from 0 to 45.

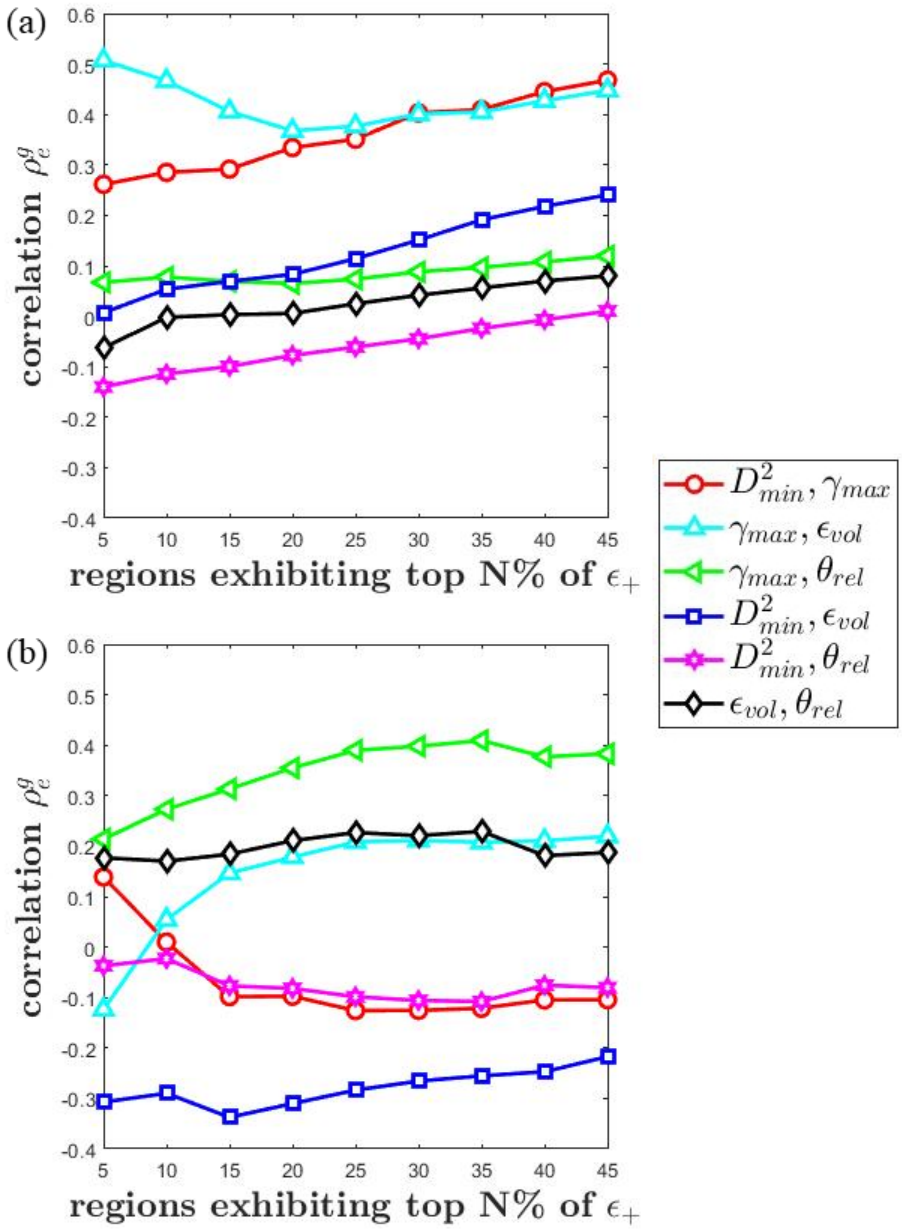

Figure 5.9: Cross-correlations between colocated rearrangements in the top $N\%$ (from largest (1%) to smallest (100%)) of all rearrangements in the shear band (bottom) and the sample under simple shear (top). Correlation coefficient between the different rearrangement measures (as calculated in (5.2)) in regions experiencing top $N\%$ (by magnitude) of (a) ϵ_+ in sample under simple shear (b) ϵ_+ in shear band. In each case, the symbols in the legend correspond to e and g in (5.2) and N goes from 0 to 45.

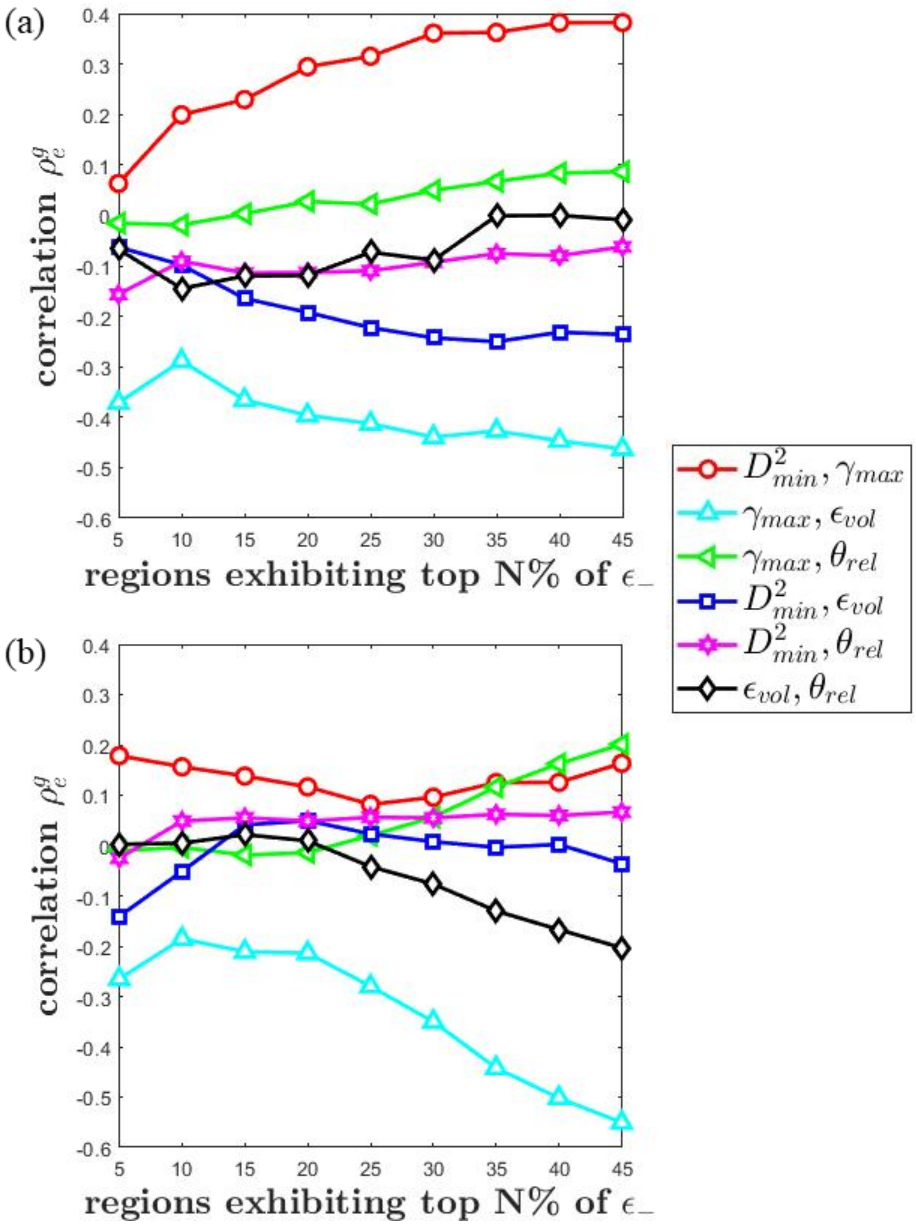

Figure 5.10: Cross-correlations between colocated rearrangements in the top $N\%$ (from most negative (1%) to least negative (100%)) of all rearrangements in the shear band (bottom) and the sample under simple shear (top). Correlation coefficient between the different rearrangement measures (as calculated in (5.2)) in regions experiencing top $N\%$ (by magnitude) of (a) ϵ_- in sample under simple shear (b) ϵ_- in shear band. In each case, the symbols in the legend correspond to e and g in (5.2) and N goes from 0 to 45.

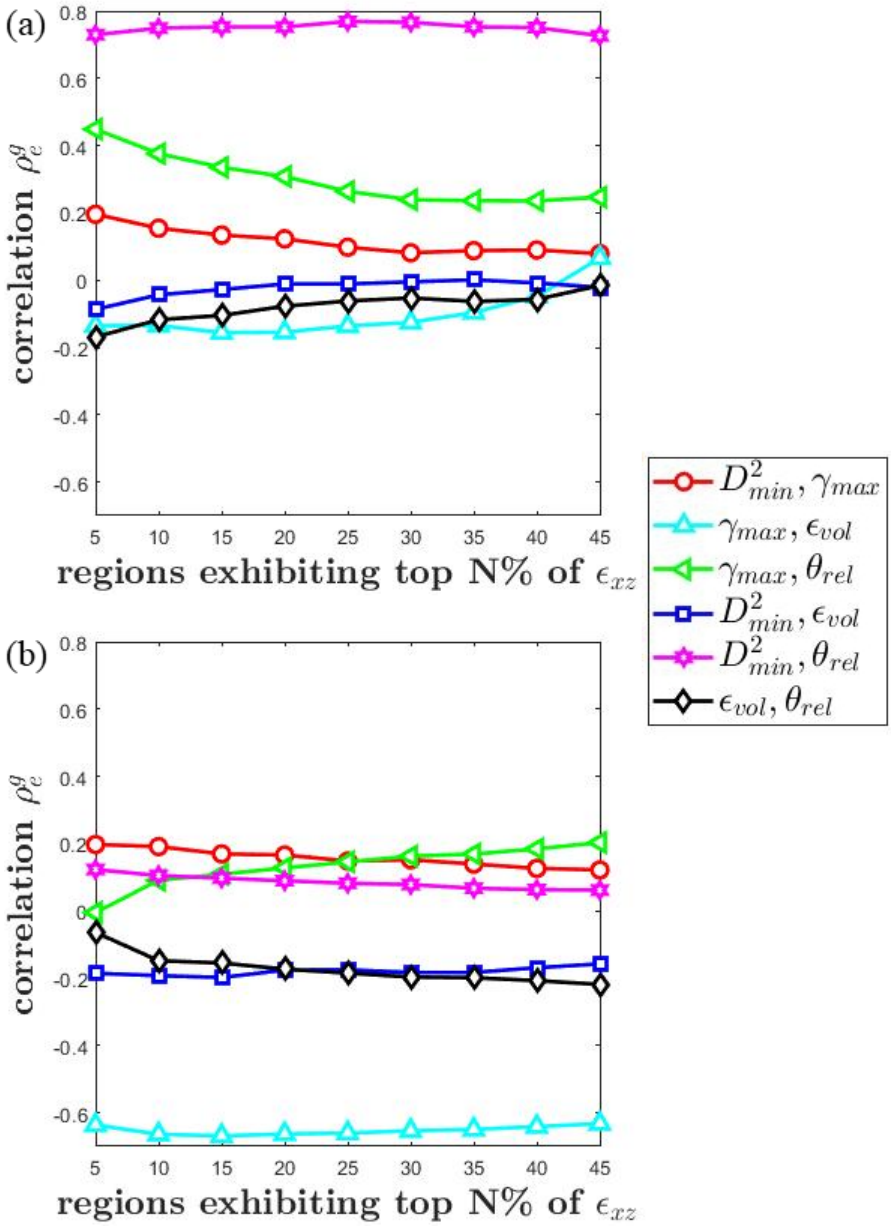

Figure 5.11: Cross-correlations between colocated rearrangements in the top $N\%$ (from largest (1%) to smallest negative (100%)) of all rearrangements in the shear band (bottom) and the sample under simple shear (top). Correlation coefficient between the different rearrangement measures (as calculated in (5.2)) in regions experiencing top $N\%$ (by magnitude) of (a) ϵ_{xz} in sample under simple shear (b) ϵ_{xz} in shear band. In each case, the symbols in the legend correspond to e and g in (5.2) and N goes from 0 to 45.

5.4 Spatial clustering of rearrangements

In Figures 5.13(a)-(d), 5.14(a)-(d), 5.12(a)-(b) we plot the locations of the regions that experience the top 15 % of rearrangement by magnitude, for all five rearrangement measures for both the shear band and the sample under simple shear. The five rearrangement measures are ordered by magnitude from the largest (1%) to the smallest (100%) (ϵ_- is ordered from most negative to least negative). We examine whether the regions that experience the most rearrangement are in the same locations in the shear band and the sample under simple shear. This can be done by simple observation since the shear band and the sample under simple shear are of the same dimensions and have about the same number of particles.

We view both the shear band and the sample under simple shear in the xz-plane (both of same dimensions). The shear band, as described previously, is a narrow, cuboidal region that is at an angle with the y-axis. This is how it is represented in the left column of figures in Figures 5.13 (a),(c), Figures 5.14(a),(c) and 5.12(a). We see in Figures 5.13 (a) and (b) that there is some spatial clustering of D^2_{min} in both the shear band and the sample under simple shear. We see that this clustering in the sample under simple shear slightly resembles that of the shear band in that, clustering occurs near the top and bottom. Although, in the shear band, this occurs only at opposite corners of the top and the bottom sections. We also see spatial clustering of γ_{max}. But this clustering is at different locations for the shear band and the sample under simple shear. As described in previous sections, a shear band has an interior region of greater shear strain than the entire shear band itself. Hence, we see that the γ_{max} clustering is near the center in the shear band. For the sample under simple shear, the clustering is near the bottom wall. For the remaining three

rearrangement measures (θ_{rel}, ϵ_+, ϵ_-), we see no particular spatial clustering in the shear band or the sample under simple shear. The locations of regions rearranging the most (as measured by the remaining three : θ_{rel}, ϵ_+, ϵ_-) is also different in the shear band and the the sample under simple shear.

Overall, we see that regions rearranging the most are at different locations in the shear band and the sample under simple shear (from all rearrangement measures) and there is no striking similarity. There is some spatial clustering in D^2_{min} and γ_{max}, which is also different in the shear band and the sample under simple shear.

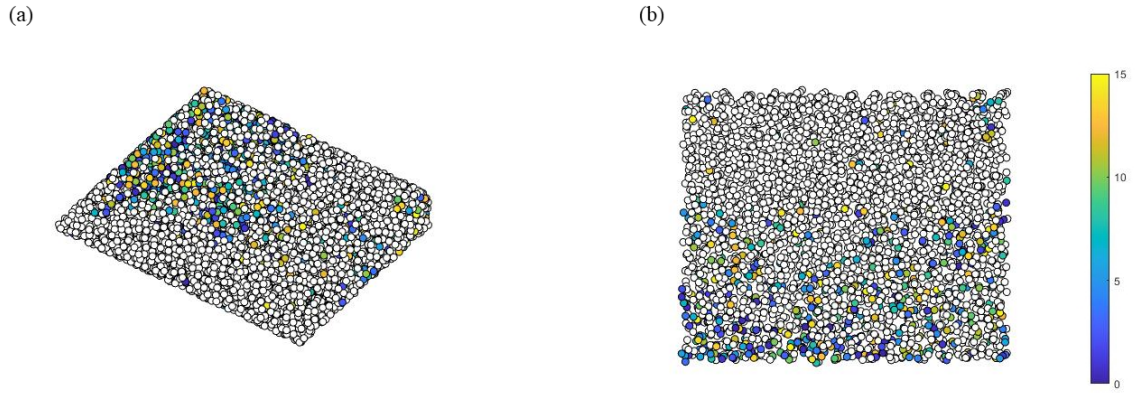

Figure 5.12: Locations of regions experiencing the top 15 %ile of θ_{rel} for both the shear band and the sample under simple shear. The θ_{rel} of the regions are ordered by magnitude from the largest (1%) to smallest (15%). The left figure is for the shear band and the right figure is for the sample under simple shear. Both are cuboidal regions that are $10d_p$ wide and $12d_p$ long with the one on the left (shear band) being angled and the one on the right not being angled. We view 2D configurations of both deformations along the y-axis (xz-plane view). Locations of regions that experience the top 15 % (by magnitude) of (a) θ_{rel} in shear band (b) θ_{rel} in sample under simple shear. The colorbar gives the magnitude of rearrangement in the corresponding regions between smallest (15% ile) and largest (1%ile).

We performed different variations of the simple shear DEM simulation with higher wall velocity, with lesser polydispersity and we also chose timesteps with timestep difference Δt from equation (3.2) at different locations in the macroscopic response

curves (Figures 3.3 (a) and (b)) and we observed similar results. We summarize our conclusions from the results that we have obtained in the next chapter.

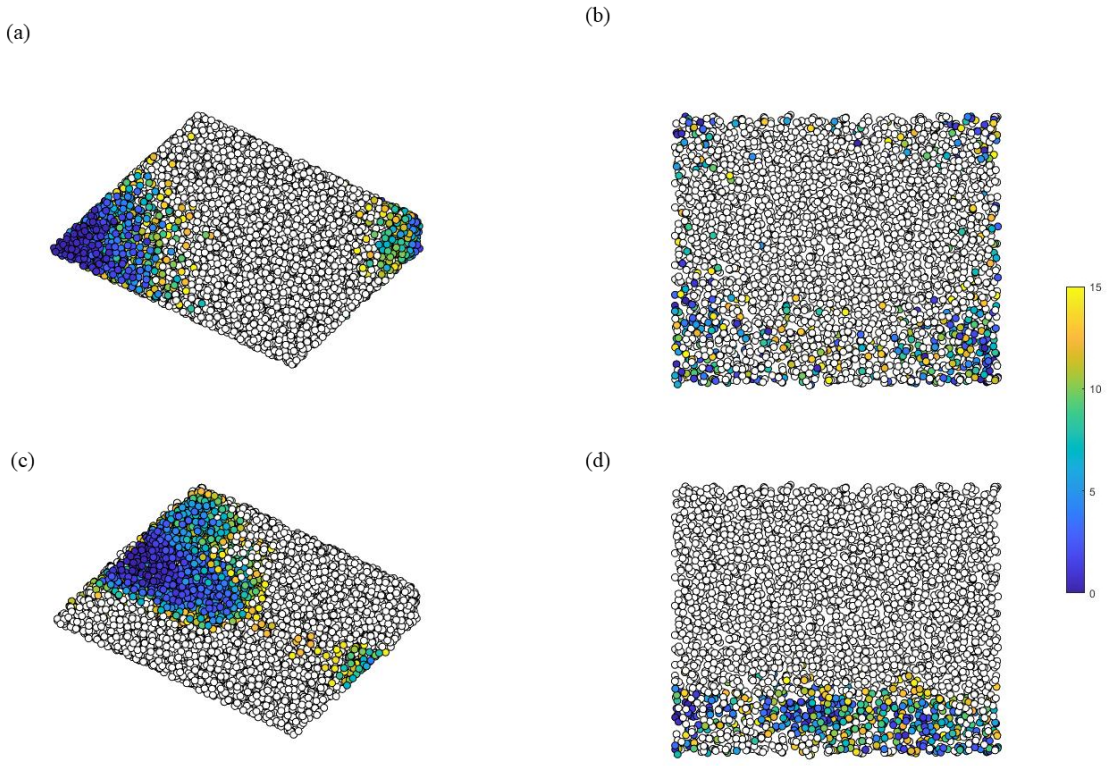

Figure 5.13: Locations of regions experiencing the top 15 %ile of rearrangements D^2_{min} and γ_{max} for both the shear band and the sample under simple shear. The rearrangements are ordered by magnitude from the largest (1%) to smallest (15%). The left column is for the shear band and the right column for the sample under simple shear. The left figures are for the shear band and the right figures are for the sample under simple shear. Both are cuboidal regions that are $10d_p$ wide and $12d_p$ long with the ones on the left (shear band) being angled and the ones on the right not being angled. We view 2D configurations of both deformations along the y-axis (xz-plane view). Locations of regions that experience the top 15 % (by magnitude) of (a) D^2_{min} in shear band (b) D^2_{min} in sample under simple shear (c) γ_{max} in shear band (d) γ_{max} in sample under simple shear. The colorbar gives the magnitude of rearrangement in the corresponding regions between smallest (15% ile) and largest (1%ile).

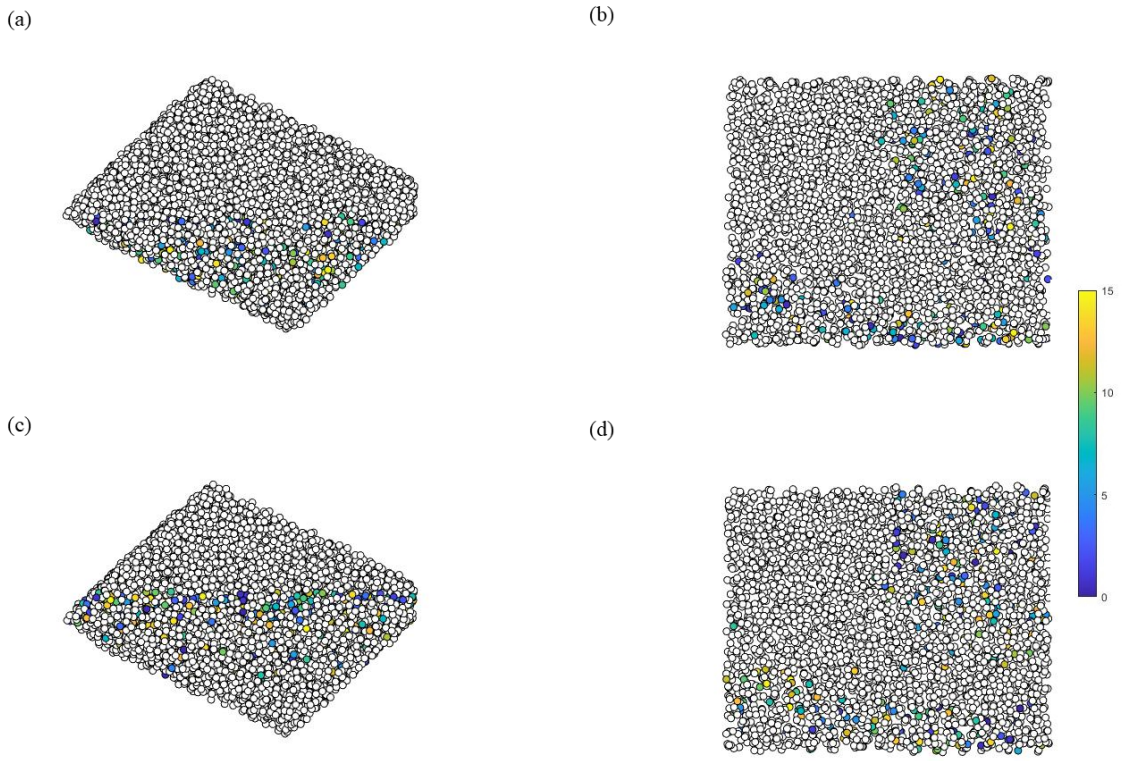

Figure 5.14: Locations of regions experiencing the top 15 %ile of rearrangements ϵ_+ and ϵ_- for both the shear band and the sample under simple shear. The rearrangements are ordered by magnitude from the largest (1%) to smallest (15%) (most negative to least negative for ϵ_-). The left column is for the shear band and the right column for the sample under simple shear. The left figures are for the shear band and the right figures are for the sample under simple shear. Both are cuboidal regions that are $10d_p$ wide and $12d_p$ long with the ones on the left (shear band) being angled and the ones on the right not being angled. We view 2D configurations of both deformations along the y-axis (xz-plane view). Locations of regions that experience the top 15 % (by magnitude) of (a) ϵ_+ in shear band (b) ϵ_+ in sample under simple shear (c) ϵ_- in shear band (d) ϵ_- in sample under simple shear.The colorbar gives us the magnitude of rearrangement in the corresponding regions between smallest (15% ile) and largest (1%ile).

Chapter 6

Discussion and conclusion

We compared the probability distributions of the five different rearrangement metrics within the shear band with an equivalent simple shear simulation. In the DEM simulation, the strain snapshot of the DEM simulation chosen is such that the homogenized microscopic strain that the central shear flowing region of the granular sample experiences is the same as that of the shear band. We see that overall, there is significantly greater non-affine deformation in the shear band than in the simple shear simulation. The local relative grain rotations are also, on an average higher in the shear band than in the sample under simple shear. The shear band also experiences greater local shear than the sample under simple shear. Even though the average of the volumetric strains ϵ_{vol} of the shear band and the simple shear simulation are the same, there is significantly greater local volumetric strain (both local dilation and local contraction) in the simply sheared granular sample. The variance of ϵ_{vol} probability distribution for the simple shear simulation is almost twice that of the shear band. So, the shear band experiences greater non-affine rearrangement, local shear and local relative particle rotations whereas the granular sample under

simple shear experiences greater local dilation and local contraction. We observe no particularly striking similarities between the rearrangement probability distributions of the two deformations.

We also see that local regions rearranging the most contribute heavily to the macroscopic strain in the sample under simple shear and the contributions are about the same as in the shear band (the highest being about 37 % from regions experiencing the most γ_{max} in the granular sample under simple shear). Perhaps the contributions from these heavily rearranging regions is the only thing that remains the same between the sample under simple shear and the shear band. Rearranging regions of the same rearrangement metric contribute about the same fraction to the macroscopic strain whether in the sample under simple shear or the shear band.

We observe slightly stronger cross-correlations between rearrangements in the shear band than in the granular sample under simple shear. We initially thought that these higher cross-correlations may be due to the higher friction in Ottawa sand. However, re-running the DEM simulations with a higher inter-particle friction coefficient does not yield stronger cross-correlations. While the trends may be similar the rearrangements are slightly more strongly correlated with one another in the shear band. This effect is particularly pronounced for the correlation between γ_{max} and ϵ_{vol}. The negative correlation between γ_{max} and ϵ_{vol} is stronger in the shear band than in the granular sample under simple shear.

In the recent paper from the Hurley research group [9], it was suggested that local rearrangements depend much more on local structure than any other quantity (such as rearrangement history, particle stresses, loading etc.). Hence, while the shear band and the granular sample under simple shear may be under similar loading, they may have significantly different structure measures, such as local porosity (ϕ),

which may explain the lack of similarity in the rearrangements between the two. We believe that since the grains in the shear band have undergone significant deviatoric loading before reaching load steps 4 and 5, the shear band fabric and structure is different from that of the granular sample under steady state simple shear. We believe the explanations for the differences in the rearrangement distributions between the shear band and the sample under simple shear lie in the difference in the structure of the granular assembly of these two deformations. We can calculate the correlation between local porosity (ϕ) at step s and step $s+1$ and any rearrangement measure in regions experiencing the top N% of rearrangement using :

$$\rho^{\phi(s)}_{e(i,s,s+1)} = \frac{\sum_{i=1}^{N\%}[e(i,s,s+1) - < e(s,s+1) >][\phi(i,s) - < \phi(s) >]}{\sqrt{\sum_{i=1}^{N\%}[e(i,s,s+1) - < e(s,s+1) >]^2}\sqrt{\sum_{i=1}^{N\%}[\phi(i,s) - < \phi(s) >]^2}} \tag{6.1}$$

In Figure 6.1, we plot the distribution of the local porosity ϕ (ratio of total volume of voids in the local averaging region to the volume of the local averaging region) at the first of the two load steps or timesteps in the shear band and the sample under simple shear. We see that the distribution of the shear band local porosity almost has twice the variance. In Figures 6.2 (a) and (b) we see the correlations between the rearrangements and the local porosity in the regions rearranging the most. We see that the rearrangements are correlated with the porosity differently in the shear band than in the sample under simple shear. The correlations are slightly stronger in the granular sample under simple shear than in the shear band. Further exploration of differences in other structure measures may help us understand the difference in local rearrangements between the shear band and the sample under simple shear.

Our major conclusion is that a shear band and a granular sample of same size,

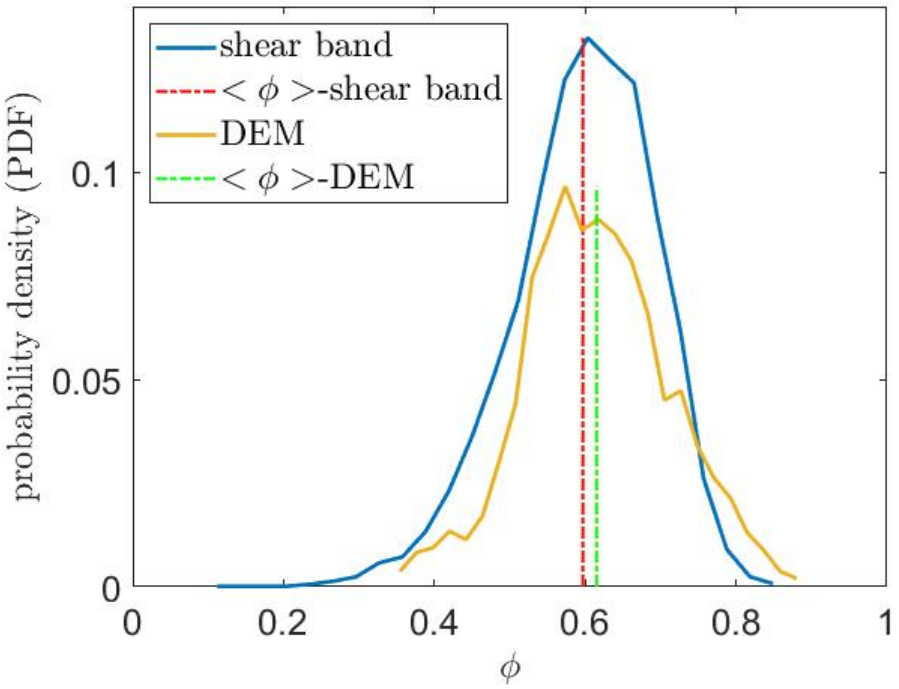

Figure 6.1: Distributions of local porosity for the granular sample under simple shear and the shear band.

with the same number of particles under simple shear experiencing the same macroscopic shear strain do not necessarily experience the same local rearrangements. Similarity in dimensions and macroscopic strain are not sufficient for the local rearrangements to be comparable. This tells us that local rearrangements in granular materials may depend much more on other characteristics such as their local structure.

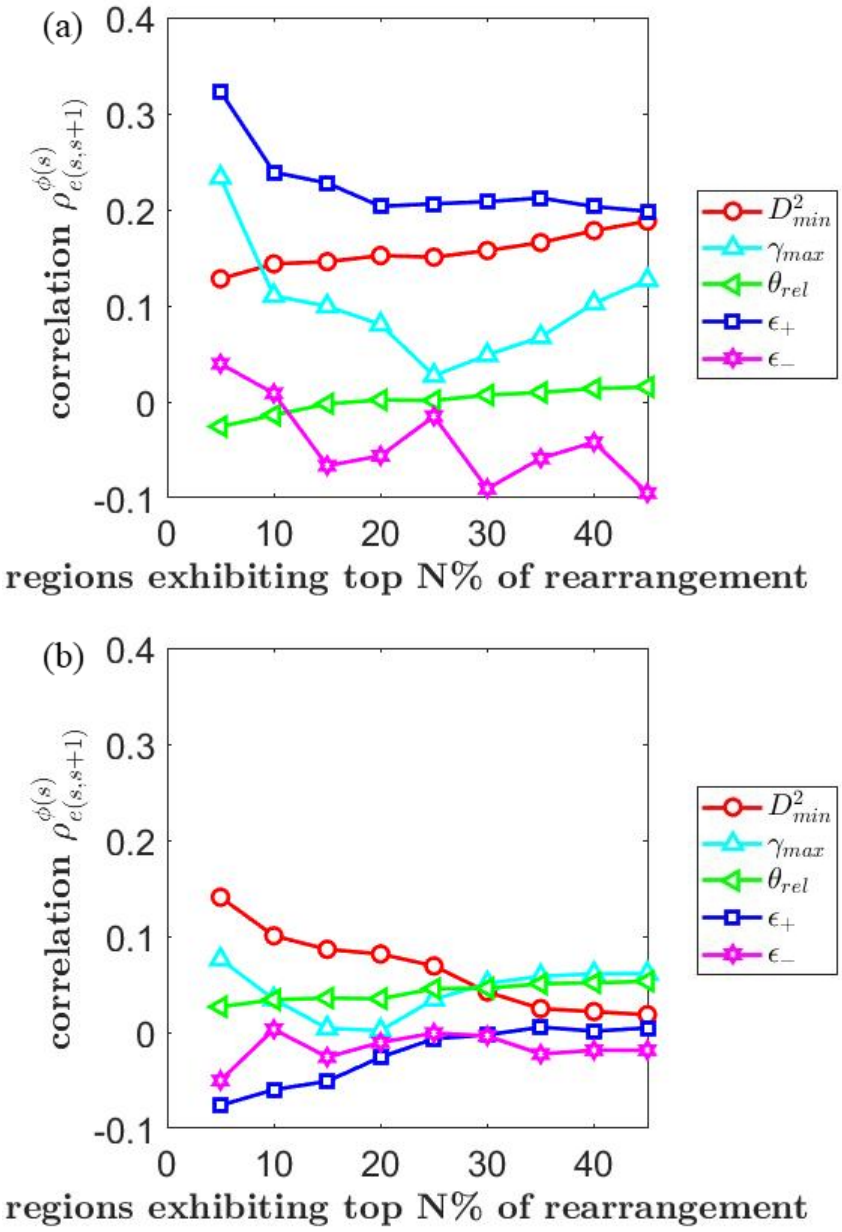

Figure 6.2: Correlation of rearrangements ($e(s, s+1)$) with local porosity $\phi(s)$ (a) for the sample under simple shear (b) for the shear band. The correlation is calculated using (6.1). In all cases, rearrangements are only considered in top $N\%$ as ordered by rearrangement magnitude from largest (1%) to smallest (100 %).

In the future, we intend to perform an in-depth analysis of the dependence of

the local rearrangements on local structure. We mentioned local porosity as one of many different structure measures in our discussion. However, there is another way of characterising the structure of the granular assembly. The granular assembly can be treated as an undirected graph or a network with the particles as nodes and the contacts between the particles as edges. Recent studies [23, 18] have proposed that network measures as structure measures probably influence the local rearrangements much more than the local porosity. We believe an in-depth exploration of the different local structure measures of granular assemblies and their influence on local rearrangements will give us more detailed insights in to the micromechanics of granular materials.

Bibliography

[1] E. Andò, S. Hall, G. Viggiani, J. Desrues, P. Bésuelle, Grain-scale experimental investigation of localised deformation in sand: A discrete particle tracking approach, Acta Geotechnica 7 (08 2012). doi:10.1007/s11440-011-0151-6.

[2] S. Hall, M. Bornert, J. Desrues, Y. Pannier, N. Lenoir, G. Viggiani, P. Bésuelle, Discrete and continuum analysis of localised deformation in sand using x-ray ct and volumetric digital image correlation, Géotechnique 60 (01 2010). doi:10.1680/geot.2010.60.5.315.

[3] J. Desrues, G. Viggiani, Strain localization in sand: an overview of the experimental results obtained in grenoble using stereophotogrammetry, International Journal for Numerical and Analytical Methods in Geomechanics 28 (4) (2004) 279–321. arXiv:https://onlinelibrary.wiley.com/doi/pdf/10.1002/nag.338, doi:https://doi.org/10.1002/nag.338.
URL https://onlinelibrary.wiley.com/doi/abs/10.1002/nag.338

[4] R. Alikarami, E. Andò, M. Gkiousas-Kapnisis, A. Torabi, G. Viggiani, Strain localisation and grain breakage in sand under shearing at high mean stress: insights from in situ x-ray tomography, Acta Geotechnica 10 (12 2014). doi:10.1007/s11440-014-0364-6.

[5] D. Chen, D. Semwogerere, J. Sato, V. Breedveld, E. R. Weeks, Microscopic structural relaxation in a sheared supercooled colloidal liquid, Phys. Rev. E 81 (2010) 011403. doi:10.1103/PhysRevE.81.011403.
URL https://link.aps.org/doi/10.1103/PhysRevE.81.011403

[6] M. L. Falk, J. S. Langer, Dynamics of viscoplastic deformation in amorphous solids, Physical Review E 57 (6) (1998) 7192.

[7] Y. Chen, M. Jiang, L. Dai, How does the initial free volume distribution affect shear band formation in metallic glass?, Science China Physics, Mechanics and Astronomy 54 (8) (2011) 1488–1494. doi:10.1007/s11433-011-4376-z.
URL https://doi.org/10.1007/s11433-011-4376-z

[8] G. Shahin, R. C. Hurley, Hp-taco: A high-pressure triaxial compression apparatus for *In-Situ* x-ray measurements in geomaterials. in preparation.

[9] C. Zhai, N. Albayrak, J. Engqvist, S. A. Hall, J. Wright, M. Majkut, E. B. Herbold, R. C. Hurley, Quantifying local rearrangements in three-dimensional granular materials: Rearrangement measures, correlations, and relationship to stresses, Phys. Rev. E 105 (2022) 014904. doi:10.1103/PhysRevE.105.014904.
URL https://link.aps.org/doi/10.1103/PhysRevE.105.014904

[10] S. Zhang, C. Zhai, K. Liu, S. Song, H. Ji, S. Shao, M. Xu, Quantitative evaluation of energy harvesting capabilities on flexoelectric and piezoelectric materials, Journal of Applied Physics 131 (6) (2022) 064101. arXiv:https://doi.org/10.1063/5.0074737, doi:10.1063/5.0074737.
URL https://doi.org/10.1063/5.0074737

[11] J. D. Eshelby, The determination of the elastic field of an ellipsoidal inclusion, and related problems, Proceedings of the royal society of London. Series A. Mathematical and physical sciences 241 (1226) (1957) 376–396.

[12] I. Einav, Breakage mechanics—part ii: Modelling granular materials, Journal of the Mechanics and Physics of Solids 55 (6) (2007) 1298–1320. doi:https://doi.org/10.1016/j.jmps.2006.11.004.
URL https://www.sciencedirect.com/science/article/pii/S0022509606001839

[13] M. B. Cil, R. C. Hurley, L. Graham-Brady, A rate-dependent constitutive model for brittle granular materials based on breakage mechanics, Journal of the American Ceramic Society 102 (9) (2019) 5524–5534.

[14] J. Desrues, G. Viggiani, Strain localization in sand: an overview of the experimental results obtained in grenoble using stereophotogrammetry, International Journal for Numerical and Analytical Methods in Geomechanics 28 (4) (2004) 279–321.

[15] D. Cantor, E. Azéma, P. Sornay, F. Radjai, Rheology and structure of polydisperse three-dimensional packings of spheres, Physical Review E 98 (5) (2018) 052910.

[16] Q. Wei, D. Jia, K. Ramesh, E. Ma, Evolution and microstructure of shear bands in nanostructured fe, Applied physics letters 81 (7) (2002) 1240–1242.

[17] B. Baudet, M. Bolton, Soil mechanics at the grain scale: Issue 1, Géotechnique 60 (2010) 313–314. doi:10.1680/geot.2010.60.5.313.

[18] F. da Cruz, S. Emam, M. Prochnow, J.-N. Roux, F. m. c. Chevoir, Rheophysics of dense granular materials: Discrete simulation of plane shear flows, Phys. Rev. E 72 (2005) 021309. doi:10.1103/PhysRevE.72.021309.
URL https://link.aps.org/doi/10.1103/PhysRevE.72.021309

[19] M. Yang, M. Taiebat, P. Mutabaruka, F. Radjaï, Evolution of granular materials under isochoric cyclic simple shearing, Physical Review E 103 (3) (2021) 032904.

[20] T.-T. Vo, Rheology and granular texture of viscoinertial simple shear flows, Journal of Rheology 64 (5) (2020) 1133–1145.

[21] O. Stamati, E. Andò, E. Roubin, R. Cailletaud, M. Wiebicke, G. Pinzón, C. Couture, R. Hurley, R. Caulk, D. Caillerie, T. Matsushima, P. Bésuelle, F. Bertoni, T. Arnaud, A. Ortega Laborin, R. Rorato, S. Yue, A. Tengattini, O. Okubadejo, G. Birmpilis, spam: Software for practical analysis of materials, Journal of Open Source Software 5 (2020) 2286. doi:10.21105/joss.02286.

[22] C. Kloss, C. Goniva, A. König, S. Amberger, S. Pirker, Models, algorithms and validation for opensource dem and cfd-dem, Progress in Computational Fluid Dynamics 12 (2012) 140 – 152. doi:10.1504/PCFD.2012.047457.

[23] C. Zhai, E. Herbold, S. Hall, R. Hurley, Particle rotations and energy dissipation during mechanical compression of granular materials, Journal of the Mechanics and Physics of Solids 129 (2019) 19–38. doi:https://doi.org/10.1016/j.jmps.2019.04.018.
URL https://www.sciencedirect.com/science/article/pii/S0022509618309098

[24] K. Bagi, Stress and strain in granular assemblies, Mechanics of materials 22 (3) (1996) 165–177.

[25] C. Rycroft, Voro++: a three-dimensional voronoi cell library in c++doi:10.2172/946741.

URL https://www.osti.gov/biblio/946741

[26] Multi-scale mechanics of granular solids from grain-resolved x-ray measurements, Proceedings of the Royal Society A: Mathematical, Physical and Engineering Sciences (Nov 2017). doi:https://dx.doi.org/10.6084/m9.figshare.c.3911920._2017.

[27] P. Schall, D. A. Weitz, F. Spaepen, Structural rearrangements that govern flow in colloidal glasses, Science 318 (5858) (2007) 1895–1899. arXiv:https://www.science.org/doi/pdf/10.1126/science.1149308, doi:10.1126/science.1149308.

URL https://www.science.org/doi/abs/10.1126/science.1149308

[28] E. D. Cubuk, S. S. Schoenholz, J. M. Rieser, B. D. Malone, J. Rottler, D. J. Durian, E. Kaxiras, A. J. Liu, Identifying structural flow defects in disordered solids using machine-learning methods, Phys. Rev. Lett. 114 (2015) 108001. doi:10.1103/PhysRevLett.114.108001.

URL https://link.aps.org/doi/10.1103/PhysRevLett.114.108001

[29] Sphere-sphere intersection, from Wolfram MathWorld.

URL https://mathworld.wolfram.com/Sphere-SphereIntersection.html

[30] L. Bocquet, A. Colin, A. Ajdari, Kinetic theory of plastic flow in soft glassy materials, Phys. Rev. Lett. 103 (2009) 036001. doi:10.1103/PhysRevLett.

103.036001.

URL https://link.aps.org/doi/10.1103/PhysRevLett.103.036001

[31] A. Peshkov, M. Girvan, D. C. Richardson, W. Losert, Reversibility of granular rotations and translations, Phys. Rev. E 100 (2019) 042905. doi:10.1103/PhysRevE.100.042905.

URL https://link.aps.org/doi/10.1103/PhysRevE.100.042905

Vita

Surya Sidhartha Kolluri was born in India on May 4th, 1997. He received his undergraduate degree in chemical engineering at the Birla Institute of Technology and Science, (BITS) Pilani, India. He completed his undergraduate thesis at the computational fluid dynamics (CFD) lab at the University of California, Santa Barbara under the guidance of Prof. Eckart Meiburg. At UCSB, he worked on double diffusion in saline water bodies. After the completion of his undergraduate program in 2019, he worked as a research assitant at the Indian Institute of Science (IISc), Bangalore. There, he was a part of the granular flow and rheology group and advised by Professor Prabhu R. Nott.

In 2020, he started his master of science in engineering program at the Johns Hopkins University. At JHU, he is a member of the Hurley research group and is advised by Professor Ryan Hurley. He is interested in the mechanical behaviour of granular materials and while at JHU, his research is focused on local rearrangements in granular materials and their influence on the macroscopic behaviour.

In the Fall of 2022, he will move on to Providence, Rhode Island to start his PhD program in mechanics of solids and structures at Brown University.